

Cellulose Derivative/Barium Titanate Composites with High Refractive Index, Conductivity and Energy Density

Andreea Irina Barzic

Institutul de Chimie Macromoleculara Petru Poni

Marius Soroceanu

Institutul de Chimie Macromoleculara Petru Poni

Razvan Rotaru

Institutul de Chimie Macromoleculara Petru Poni

Florica Doroftei

Institutul de Chimie Macromoleculara Petru Poni

Mihai Asandulesa (✉ asandulesa.mihai@icmpp.ro)

Institutul de Chimie Macromoleculara Petru Poni <https://orcid.org/0000-0002-3459-7015>

Valeria Harabagiu

Institutul de Chimie Macromoleculara Petru Poni

Research Article

Keywords: polymer composites, refractive index, transparency

Posted Date: May 10th, 2021

DOI: <https://doi.org/10.21203/rs.3.rs-467926/v1>

License:  This work is licensed under a Creative Commons Attribution 4.0 International License.

[Read Full License](#)

Version of Record: A version of this preprint was published at Cellulose on January 9th, 2022. See the published version at <https://doi.org/10.1007/s10570-021-04343-2>.

1 **CELLULOSE DERIVATIVE/BARIUM TITANATE COMPOSITES WITH HIGH**
2 **REFRACTIVE INDEX, CONDUCTIVITY AND ENERGY DENSITY**

3

4 Andreea Irina Barzic, Marius Soroceanu, Razvan Rotaru, Florica Doroftei, Mihai Asandulesa*,

5 Valeria Harabagiu

6

7 "Petru Poni" Institute of Macromolecular Chemistry, 41A Grigore Ghica Voda Alley, 700487 Iasi,
8 Romania

9

10 **Abstract:** High refractive index and transparent materials are useful in various technical domains,
11 ranging from energy sector to microelectronics. This work deals with polymer composites prepared
12 by embedding small amounts of barium titanate in hydroxypropyl cellulose matrix. Optical
13 transparency of the composite films varies in agreement with polymer doping level. Light
14 dispersion in the prepared composites allowed evaluation of specific parameters, which are related
15 to the sample structural order and possible optical transitions. Conductivity of the composites is
16 increased due to ceramic particle addition in the polymer. Dielectric studies reveal that the prepared
17 materials are suitable for electric energy storage applications.

18

19 Keywords: polymer composites, refractive index, transparency

20

21

22

23

24

25

26

27

28

29

30

31

32

* Correspondence to: M. Asandulesa; e-mail: asandulesa.mihai@icmpp.ro

33

34 **1. INTRODUCTION**

35

36 In the global context of resource lessening, energy increasing demands and planet pollution, the
37 topics of polymer science are more and more concerned with replacing parts of high-tech products
38 with others that are striving to match the demands of low-carbon society (Zhang et al., 2019).
39 Hence, in order to alleviate the environmental burden, it is imperative to develop biodegradable,
40 less toxic and advanced materials for many technical areas, like high power electronics and energy
41 storage. In the past years, film dielectric capacitors with high energy density opened fresh
42 perspectives due to lightweight, flexible, and elevate power densities (i.e. rapid discharge of stored
43 electric energy). For such purposes, the performance of the material can be controlled via dielectric
44 constant and breakdown strength by combining plastics with inorganic fillers.

45 Barium titanate (BT) is an inorganic lead-free ferroelectric compound, which is well known in
46 materials science for its photorefractive and piezoelectric properties (Takenaka, 2013). Other
47 essential characteristics of this ceramic material are: high polarization ($\sim 26 \mu\text{C cm}^{-2}$) (Takenaka,
48 2013) and elevated permittivity (100–2000) (Petrovsky et al., 2008), quite large band gap of 3.2 eV
49 (Yogamalar et al., 2018), and relatively high piezoelectric strain constant ($\sim 190 \text{ pC/N}$) (Yogamalar
50 et al., 2018; Zhang et al., 2019). Since most of these features are rarely encountered in polymer
51 materials, BT is widely used as filler for fabrication of polymer micro/nano-composites. Therefore,
52 the utility of BT-reinforced polymers has expanded very fast in various areas of technology and
53 industry. Among them applications in energy storage (Yao et al., 2018; Yue et al., 2019), sensors
54 (Yang et al., 2020), embedded capacitors (Goyal et al., 2013), high refractive (Nagao et al., 2011)
55 and nonlinear optics coatings, are included (Mimura et al., 2010). The extent of the modification of
56 the polymer properties by BT filler is affected by the level of its dispersion inside the matrix as well
57 as by the size of the BT particles (Gu et al., 2019). An essential aspect of such composites is related
58 to the possibility to upgrade the desired properties at very small filler loadings inserted in the
59 polymer phase (Sen et al., 2016; Yue et al., 2019).

60 Several types of polymer matrices were used for preparation of BT-reinforced micro/nano-
61 composites as a function of desired balance of properties imposed by application. BT/epoxy resin
62 films were synthesized via a complex alkoxide procedure and showed a dielectric constant of 10.8
63 at 30% filler (Kobayashi et al., 2010). Poly(vinylidene fluoride-trifluoroethylene)/BT composites
64 were analyzed by polarization–electric field method, showing improved ferroelectric properties,
65 which are suitable for nonvolatile memory devices (Valiyaneerilakkal et al., 2015). Nanocomposites
66 containing BT filler were prepared by solvent casting and by using as matrix a blend of

poly(ethylene oxide) and poly(vinyl pyrrolidone) doped with LiClO₄ (Kesavan et al., 2015). The increase of ceramic filler amount has positively influenced the ionic conductivity and the thermal stability as demanded by lithium battery applications (Kesavan et al., 2015). Polyethylene oxide/BT/LiClO₄ composites, analyzed by impedance spectroscopy, revealed a conductivity of 7.6 10⁻⁶ S/cm owing to the powerful interactions between polymer and ceramic nanoparticles (Malathi et al., 2015). Such materials are candidates for solid-state polymer batteries and fuel cells. BT nanoparticles were also inserted in ethyl cellulose up to 13 vol%, leading to materials with enhanced dielectric constant (~7.5 at 1 Hz), high dielectric loss and raised dc conductivity. At low amount of reinforcements and below 60°C, the composites are good for antistatic applications, whereas above 7 vol% of BT and at high temperatures the films are suitable for electrostatic dissipation purposes (Ali et al., 2017). BT-acrylic hybrid materials produced by photopolymerization were shown to display dielectric constants that range almost linearly with nanoparticle loading up to 76 at 1 kHz at 50 wt% filler (Lombardi et al., 2011). The dielectric properties of these composites are adequate for capacitor applications. Olmos and co-workers (Olmos et al., 2013) reported the influence of processing conditions and of BT filler amount on morphology of polyvinylidene fluoride, proving that the milling process is the main factor to enhance the percent of β-phase being advantaged by the presence of BT particles. Also, the matrix lamellar aspect ratio is enhanced by the amount of filler (Olmos et al., 2013). Piezoelectric polyamide-11/BT composites were achieved by using solid-state mechanochemical procedure (Hua et al., 2019). A linear dependence was found between piezoelectric strain coefficient and filler loading, reaching 6.6 pC/N at 50 vol% BT. These composites displayed good mechanical resistance, being ideal for sensor applications. Composites with high permittivity were prepared by adding BT in polyimide and processing by electrospinning (Xu et al., 2016). The resulted hybrid nanofiber sheets reached a dielectric constant of 29.7 when the percent of BT was 50 vol%, being adequate for embedded capacitors or energy-storage uses (Xu et al., 2016). Other studies were focused on preparation of multiphase polymer nanocomposites by addition of BT and other kinds of fillers. Thus, polyimide/SiO₂-BT composites were proved to have high thermal stability (Gao et al., 2008). Ternary NiNb₂O₆/BT/poly(arylene ether nitriles) composites obtained via solution casting technique, showed great improvements at 40 wt% filler in terms of tensile properties and dielectric constant (~ 15.3 at 1 kHz), being suitable candidates for organic capacitors (Huang et al., 2020). Most reported studies are focused on structural, morphological, thermal and dielectric properties of BT-polymer composites and very few address aspects related to their optical properties (Mimura et al., 2010; Nagao et al., 2011; Morsi et al., 2019). This is probably because, at high BT loadings, the transparency of the material is compromised and limits the possibility of material investigation.

101 Optical absorption features, particularly the absorption edges are essential for describing optical
102 transitions, the band structure, the band tail and the band gap energies of composite materials. To
103 our knowledge, only the study of Morsi *et al.* (Morsi et al., 2019) describes optical constants of BT
104 composites with polyethylene oxide/carboxymethyl cellulose (PEO/CMC) as matrix. Based on
105 optical and electrical data they show that such materials can be used for sensors, electromechanical
106 transducers or as ceramic capacitors. On the other hand, Nagao *et al.* (Nagao et al., 2011)
107 demonstrates that the incorporation of BT in poly(methyl methacrylate) increases both the refractive
108 index and the permittivity of the composites, with potential use in displays and other electronic
109 devices.

110 Previously, we have prepared viscose fiber/BT composites of low BT content and proved the
111 appropriateness of their properties for applications as absorbent materials in electromagnetic fields
112 (Rotaru et al., 2016). In this work, new BT composites with biodegradable hydroxypropyl cellulose
113 (HPC) matrix were prepared. Structural, optical and electrical properties were analyzed to
114 demonstrate their usefulness for energy storage. The performed investigations will prove that the
115 HPC/BT materials have higher refractive index than PMMA/ethylene glycol monovinyl ether/BT
116 (Mimura et al., 2010) as well as larger permittivity and conductivity in comparison with
117 PEO/CMC/BT (Morsi et al., 2019) and polypropylene/BT composites (Yao et al., 2018). Energy
118 density evaluations reveal similar values to those reported for polyimide/BT composites (Yue et al.,
119 2019).

120

121 **2. EXPERIMENTAL**

122

123 **2.1 Materials**

124

125 KlucelTM Hydroxypropyl cellulose (HPC) of 100 000 g/mol molar mass and substitution degree of
126 2.5 was purchased from Aqualon Company.

127 Barium carbonate and titanium dioxide were purchased from Sigma Aldrich and used as received.

128

129 **2.2 Preparation of BT**

130

131 Barium titanate (BT) was prepared by using a wet-state reaction under ultrasonic irradiation. The
132 detailed procedure is described in a previous work (Rotaru et al., 2017). Shortly, a 1/2 (w/w)
133 titanium dioxide / barium carbonate mixture was ultrasonically irradiated at 20 kHz frequency, in
134 Milli-Q ultrapure water for 60 minutes (119 kJ energy were dissipated and the temperature reached

135 92°C) by using a generator equipped with probe and sensor for temperature. The obtained powder
136 was further decanted and dried in a microwave furnace for 10 minutes. The last step was the
137 thermal treatment for 3 hours, performed in a laboratory furnace at temperatures of 500°C.

138

139 **2.3 Preparation of HPC/BT composite films**

140

141 Film sample preparation was done as follows: a stock polymer solution was obtained by dissolving
142 5g HPC in 250 ml of deionized water at room temperature. 50 mL of HPC solution and known
143 amounts of BT particles of different filler loadings (0.5, 1 and 2 % BT) were homogenized by
144 ultrasonication for 10 minutes; during this procedure, 7 kJ energy was dissipated and the
145 temperature increased from 20°C to 40°C. The prepared dispersions were poured onto Petri dishes
146 of 10 cm diameter. The films were obtained by drying overnight at room temperature and then they
147 were kept in a vacuum oven at 90°C for 6 hours. The pure HPC film was obtained by using a
148 similar procedure.

149 The thickness of the obtained HPC and composite films ranged between 70 to 140 µm as measured
150 with a digital micrometer.

151

152 **2.4 Characterization**

153

154 The structures of barium titanate (BT) powder, pristine HPC film and the HPC/BT composites films
155 were investigated by FTIR spectroscopy in potassium bromide pellets using a BrukerVertex 70
156 Spectrometer.

157 In order to highlight the morphology of the samples, they were examined on the surface and in
158 cross-section. Surface morphology for the control HPC sample and HPC/BT composites were
159 analyzed on a Verios G4 UC scanning electron microscope (SEM) from Thermo Scientific, Czech
160 Republic. The samples were coated with 10 nm platinum using a Leica EM ACE200 Sputter coater
161 to render electrical conductivity and to obstruct charge buildup during exposure to the electron
162 beam. SEM investigations were performed in high vacuum mode using a secondary electron
163 detector (Everhart-Thornley detector, ETD) at accelerating voltage of 5 kV. Cross-sectional
164 analysis of films was performed on a Quanta 200 device (FEI, Czech Republic). To achieve the
165 cross section, the films were immersed in liquid nitrogen to impede deformation during fracture.
166 The presence of the BT was confirmed by energy dispersive X-ray (EDX) analysis using the Quanta
167 200 microscope coupled with EDX detector.

168 UV-VIS features of the free-standing films were examined on a SPECORD 210 PLUS device.

169 Refraction properties of film samples were measured on a DR-M4 Abbe refractometer at several
170 wavelengths from visible range.

171 Dielectric measurements were carried out on a broadband dielectric spectrometer equipped with a
172 high resolution Alpha-A analyzer. The dielectric spectra were recorded at room temperature, in a
173 frequency range between 1 Hz and 10^6 Hz.

174

175 **3. RESULTS AND DISCUSSION**

176

177 HPC was used as matrix for the preparation of organic-inorganic composites of different BT
178 contents. To obtain optically transparent composites a maximum of 2% of BT filler was used.

179

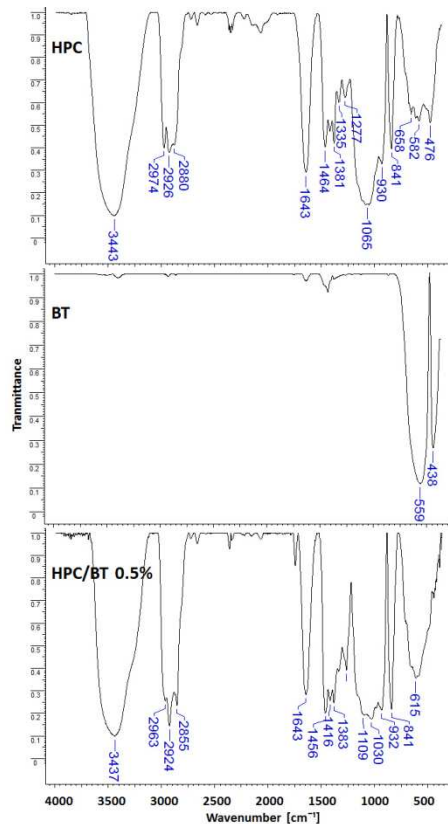
180 **3.1 FTIR analysis**

181

182 The structures of the precursors and the composites were first assessed through FTIR spectroscopy
183 (Figure 1). As observed from Figure 1, HPC displays prominent bands at 1049, 1057, 1080 cm^{-1}
184 corresponding to $-\text{C}-\text{O}-\text{C}-$ stretching, while those noticed at 1643, 3443 cm^{-1} and at 658, 582, 476
185 cm^{-1} are assigned to $-\text{OH}$ stretching and to out of plain bending of C-OH units. The bands in the
186 region 2880-2974 cm^{-1} and that centered at 1464 cm^{-1} are attributed to C-H stretching, respectively
187 to C-H in-plane bending vibrations. Other spectral bands, such as, 1335 cm^{-1} (CH_2 rocking vibration
188 at C6), 1381 cm^{-1} (CH in-plane bending), 1418 cm^{-1} (HCH in plane bending vibration, CH_2
189 scissoring motion, CH_2 symmetric bending at C6) are also attributed to alkyl units of the cellulose
190 chain (Sharma et al., 2009; Abdel-Halim et al., 2015; Joshi et al., 2019).

191 The infrared spectrum of BT shows characteristic bands at 438 cm^{-1} and 559 cm^{-1} . The band
192 observed at lower wavenumber (438 cm^{-1}) is one of the “fingerprints” of BT and it is attributed to
193 the Ba–O and Ti–O metal oxides vibration. The presence of the band at higher wave number (559
194 cm^{-1}) is ascribed to Ti–O₁ normal stretching vibration (characteristic to BaTiO₃ tetragonal phase)
195 (Rotaru et al., 2016). The FTIR spectrum of the composite with a content of 0.5% BT filler, shown
196 as a typical one for all HPC/BT samples presents all characteristic bands of HPC matrix, while the
197 “fingerprints” of the filler are superposed with COH out-of plane bending vibrations of HPC in a
198 large and high intensity band, centered at 615 cm^{-1} .

199



200

201 **FIGURE 1** FTIR spectra of HPC film, BT powder, and HPC/BT 05% composite films

202

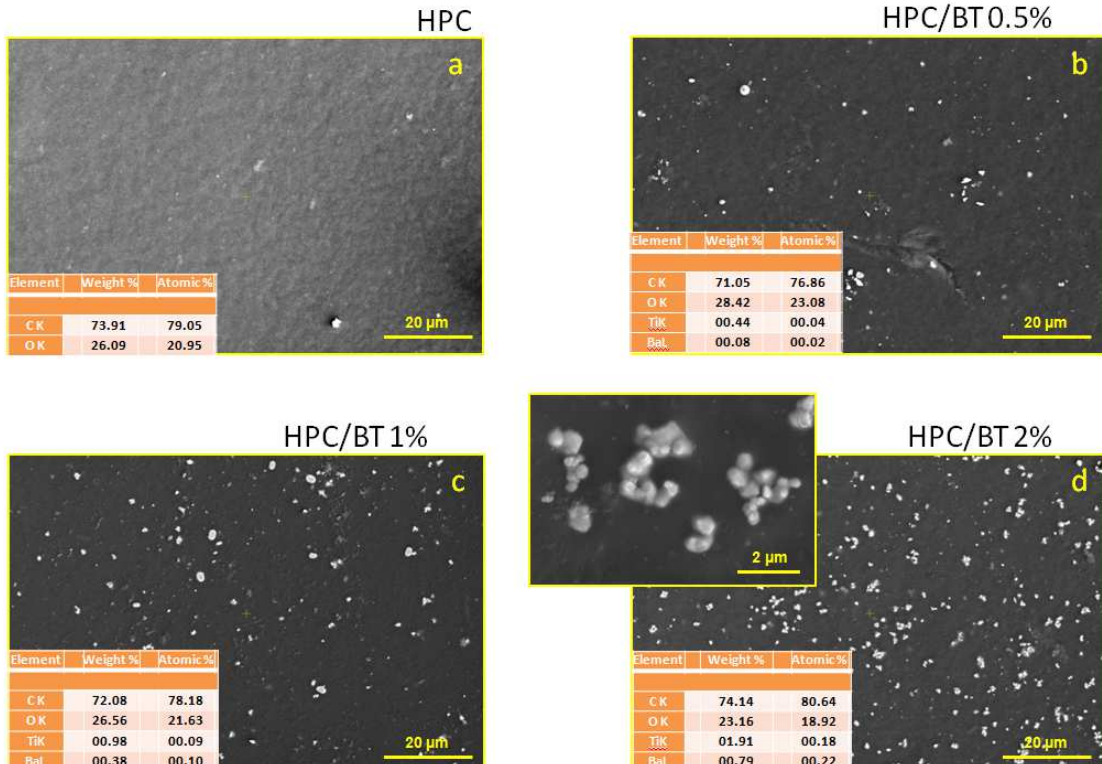
203 **3.2 Morphology**

204

205 The morphological investigations were made by SEM coupled with EDX for the neat HPC and BT
 206 filled films. Figure 2 shows the surface micrographs and EDX compositional results. The HPC
 207 matrix displays mainly a relatively textured surface sprinkled with small defects probably formed
 208 due to partially crystalline nature of cellulose material (Vanderghem et al., 2012; Mohd Ishak et al.,
 209 2020). In a previous work (Rotaru et al., 2016), the morphology of the used BT powder was found
 210 to consist in agglomerated particles having almost spherical shape, while their diameters varied
 211 between 550-1300 nm. Here, these ceramic particles can be easily observed as white approximately
 212 spherical dots which are present for all filler concentrations and with increasing particles' density
 213 on the film surface with increasing BT content. The ceramic filler is well and uniformly dispersed
 214 within the cellulose derivative matrix on the surfaces of the samples. Relatively similar morphology
 215 was noted for BT/polyaniline composites (Pant et al., 2006).

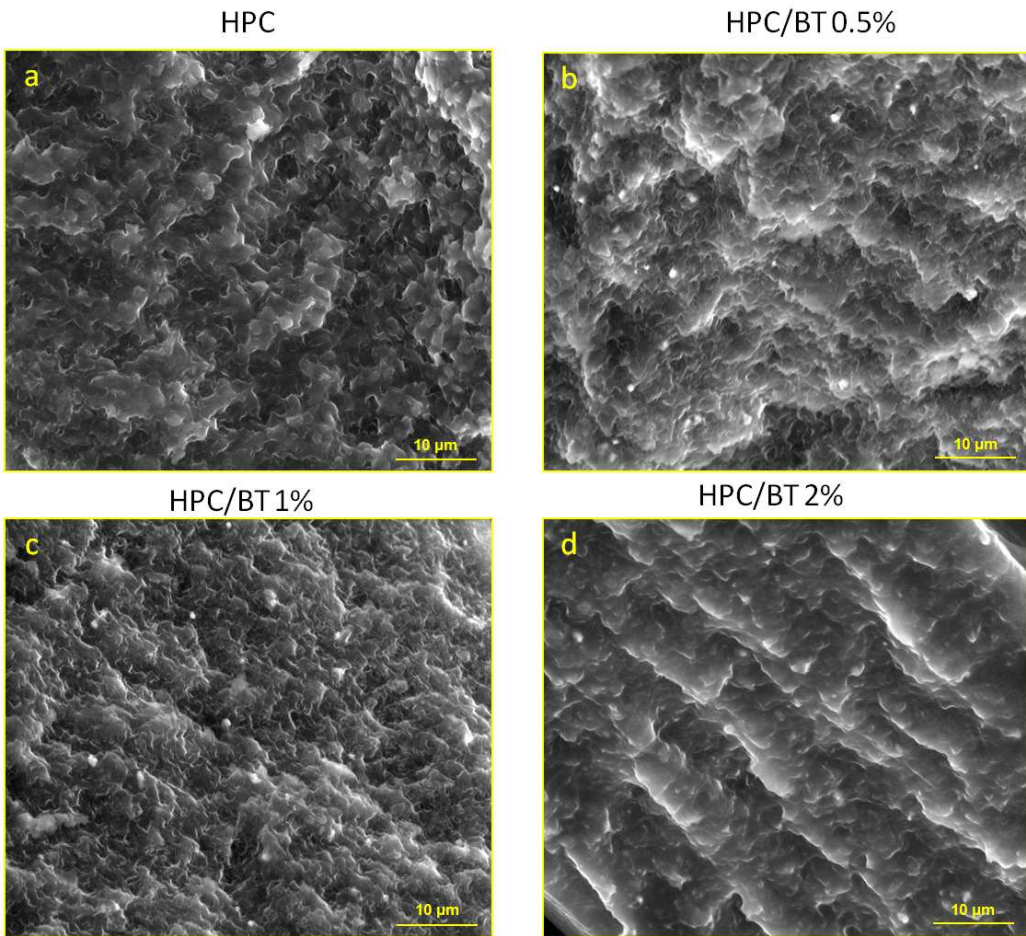
216 The qualitative results on film compositions provided by the EDX analysis are presented in the
 217 tables inserted in Figure 2. EDX recordings show the lack of Ba and Ti elements on the surface of
 218 pristine HPC, while, upon reinforcement, the percentage of these chemical elements is closed to the

219 content of BT filler in each composite sample. EDX analysis is a volume analysis which means that
220 the ceramic BT particles dispersion is uniform not only on the surface but also inside the reinforced
221 polymer films.



222
223 **FIGURE 2** SEM micrographs of the surface of HPC and HPC/BT composites: (a) HPC, (b)
224 HPC/BT 0.5%, (c) HPC/BT 1% and (d) HPC/BT 2%

225
226 Cross-section SEM images of HPC and HPC/BT samples are depicted in Figure 3. HPC, known for
227 its thermotropic liquid crystalline behavior generated a film which displayed a granular structure,
228 with small pores, typical for a three-dimensional network (Nishio & Takahashi, 1984; Silva et al.,
229 2008). The incorporation of small amounts (0.5, 1 %) of BT in the HPC matrix does not change this
230 morphology. However, when 2 % BT were added into HPC matrix, a pleated morphology of the
231 cross-section of the resulted film was observed. Moreover, HPC/BT films show more compact
232 morphology with a lower porosity as compared to the pristine HPC film, especially for HPC/BT 2%
233 sample, also evidenced by decreasing values of film thickness as a function of BT content (Table 1).
234 Increased compactness of the composite films was earlier evidenced by Banerjee *et al.* (Banerjee et
235 al., 2019) for poly(vinyl alcohol)/ manganese chloride composites.
236



237

238 **FIGURE 3** SEM micrographs: Cross-sections of HPC and HPC/BT composites films: (a) HPC, (b)
 239 HPC/BT 0.5%, (c) HPC/BT 1% and (d) HPC/BT 2%

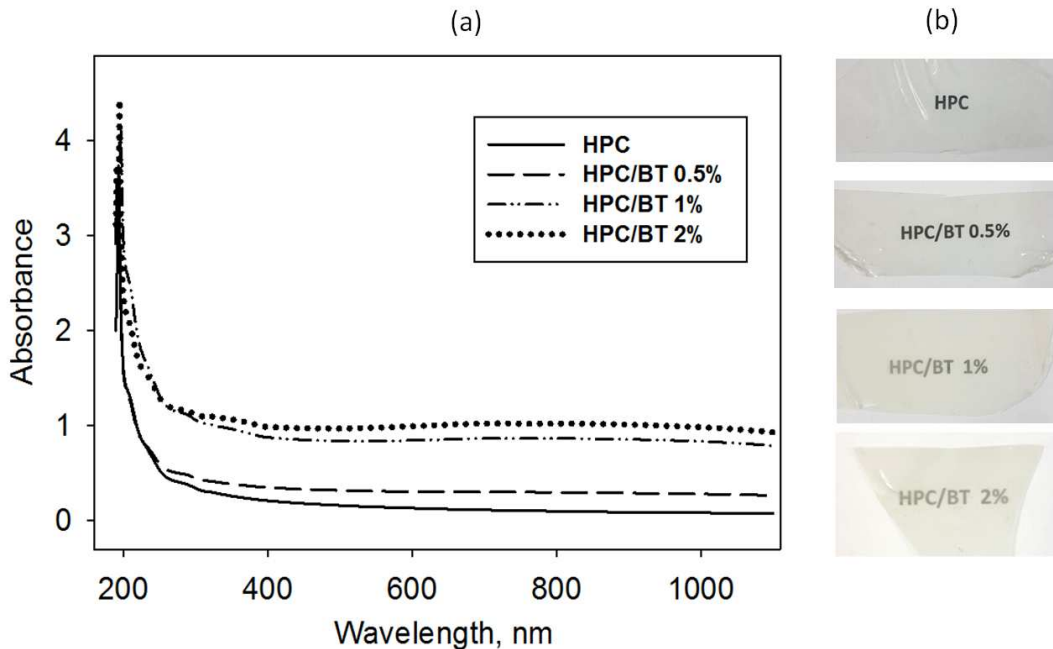
240

241 **3.3 Absorption edge and band gap energies**

242

243 The transparency properties of HPC and HPC/BT composite samples were investigated by UV-
 244 VIS-NIR spectroscopy on free-standing films. Figures 4a and b show the spectra samples. A sharp
 245 absorption edge is noticed in the spectrum of the cellulosic matrix, which is slightly enhanced by
 246 the addition of BT particles in the HPC matrix. The observed absorbance behavior of the prepared
 247 composite samples presents changes in the magnitude of the optical band gap energy with further
 248 loading of BT filler in the system, reflecting the possible interactions between the two phases.
 249 Similar spectral features were reported by Morsi *et al.* (Morsi et al., 2019) for composites of
 250 PEO/CMC filled with BT particles. For the investigated samples, the optical clarity of the prepared
 251 materials is gradually diminished and the absorbance is enhanced as BT loading increases from 0%
 252 to 2% in the HPC matrix. Thus, the reinforcement of the composite films favors light scattering and
 253 enhances the absorption coefficient. This aspect can be observed from a simple visual examination

254 of the free-standing films, since their aspect gradually changes from transparent to almost white
 255 color (Figure 4b). Absorption and scattering phenomena caused by 1% and 2% BT reinforcement of
 256 cellulose derivative are altering the transparency of pristine HPC film.



257
 258 **FIGURE 4** UV-VIS-NIR spectrum of the neat HPC and HPC/BT composite films (a) and the
 259 pictures of analyzed samples (b)

260
 261 The optical absorption coefficient characterizes the material ability to absorb electromagnetic
 262 radiations, particularly from visible range. Optical absorption coefficient was estimated for each of
 263 the investigated samples by introducing UV-VIS data in equation (1):

$$264 \quad \alpha = \frac{1}{t} \ln \left(\frac{1}{T} \right) \quad (1)$$

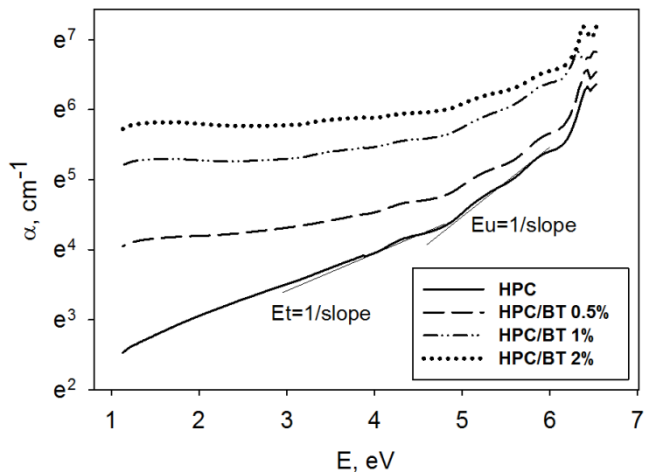
265 where α is the optical absorption coefficient, t is the thickness of the film sample and T is the
 266 transmittance.

267 For all spectra illustrated in Figure 4a, the absorption edge, representing the low energy wing of the
 268 first absorption band, is analogous to the edge suggested by Tauc approach (Tauc, 1967) for ideal
 269 amorphous semiconductors. Given this similarity, the absorption edge parameters were determined
 270 from the dependence of absorption coefficient on photon energy, as depicted in equation (2):

$$271 \quad \alpha \sim \exp \frac{E}{E_0} \quad (2)$$

272 where E is the photon energy ($E=hu$), E_0 can be either Tauc energy (E_t) or Urbach energy (E_u).
 273 Graphical representations of equation (2) as semi-logarithmic plots are following the Urbach
 274 relation as shown in Figure 5. Absorption edge energies were extracted from the reverse of slopes

275 of the straight lines and the results are listed in Table 1. Et is the optical parameter extracted from
 276 the low-energy exponential zone of the dependence of absorption coefficient on photon energy,
 277 while Eu is related to the high-energy exponential region. For pristine HPC matrix, as well as for
 278 HPC/BT composites the values of Et are higher than those of Eu. Therefore, the absorption related
 279 to possible structural defects (i.e. break or torsion of polymer chains) is more pronounced with
 280 regard to absorption determined by structural disorder. No report on Eu and Et was found in
 281 literature for polymer/BT composites. Moreover, BT reinforcement generates intensification of
 282 these absorption processes as seen in the increase of Et and Eu parameters.



283

284 **FIGURE 5** Optical absorption coefficient versus photon energy for unfilled HPC and HPC/BT
 285 composite films

286

287 **TABLE 1** The values of the film thickness, Tauc energy (Et), Urbach energy (Eu), indirect band
 288 gap (Egi) and direct band gap (Egd) values for pristine HPC and HPC/BT composites

Sample code	Thickness, μm	Et, meV	Eu, meV	Egi, eV	Egd, eV
HPC	140	2046	1166	5.71	6.12
HPC/BT 0.5%	110	3294	1363	5.43	6.03
HPC/BT 1%	100	4474	1570	5.31	5.96
HPC/BT 2%	70	6858	2181	5.20	5.81

289

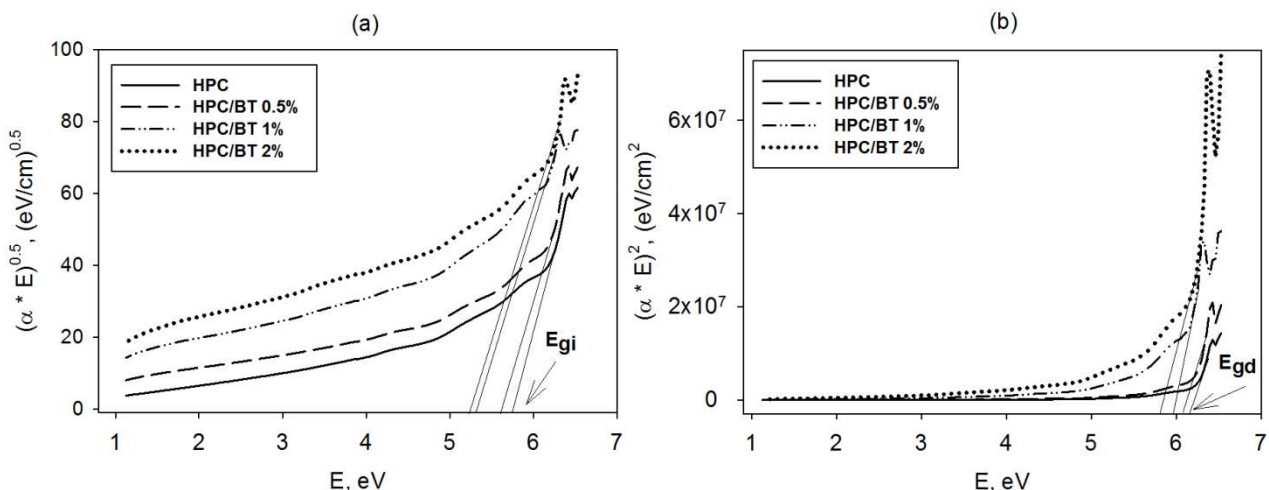
290 The photon energy that is demanded for transporting the electrons from the valence to the
 291 conduction band can be estimated by examining the region of the absorption boundary. Based on
 292 literature data (Choudhary & Sengwa, 2018; Morsi et al., 2019; Sengwa et al., 2019), it is well
 293 known that the majority of photon absorbing materials are characterized by a direct and an indirect

band gap close to fundamental absorption edge. The theory proposed by Tauc (Tauc, 1967) allows the calculation of the band gap energy (E_g), as expressed by equation (3):

$$\alpha E = C(E - E_g)^m \quad (3)$$

where C is a constant and m is a parameter that describes the nature of the electronic transitions, taking the value of 0.5 for direct allowed transitions and 2 for indirect allowed transitions.

Figure 6 displays the plots of $(\alpha E)^{1/m}$ versus photon energy for $m=0.5$ and $m=2$. Linear parts are noticeable in all plots and their intersection with x-axis is essential for establishing the E_g values for the prepared samples. Electrons travelling from the valence to the conduction band, while conserving total energy and the wave-vector k-space, denotes a direct transition. On the other side, electron moving in the conduction band at distinct k-spaces produces an indirect transition. The estimated values of indirect band gap (E_{gi}) and direct band gap (E_{gd}) for the investigated samples are illustrated in Table 1. Regardless the filling level of HPC, the results indicate lower values for E_{gi} as compared to E_{gd} . Moreover, the reduction of optical band gap energy with enhancement of inorganic filler loading was registered, a common feature for polymer composites (Choudhary & Sengwa, 2018; Morsi et al., 2019; Sengwa et al., 2019). The obtained band gap values for HPC/BT are slightly higher than those reported by Morsi *et al* (Morsi et al., 2019) for PEO/CMC filled with BT. The presence of ceramic BT particles within HPC matrix facilitates electron crossing in the valence band with production of supplementary localized energy states in the forbidden energy zone and therefore lowering the band gap of the BT/HPC materials. The E_g reduction for composites with the variation in content of the constituting phases is believed to enhance with the degree of disorder (higher Eu) in the material, which determines an increase in the flexibility of the macromolecular chains. Hence, the charge carriers, particularly at higher reinforcement degrees have better mobility and the electrical features will improve.



318 **FIGURE 6** Plots of $(\alpha E)^{0.5}$ versus E (a) and $(\alpha E)^2$ versus E (b) for pristine HPC and HPC/BT
319 composite films

320

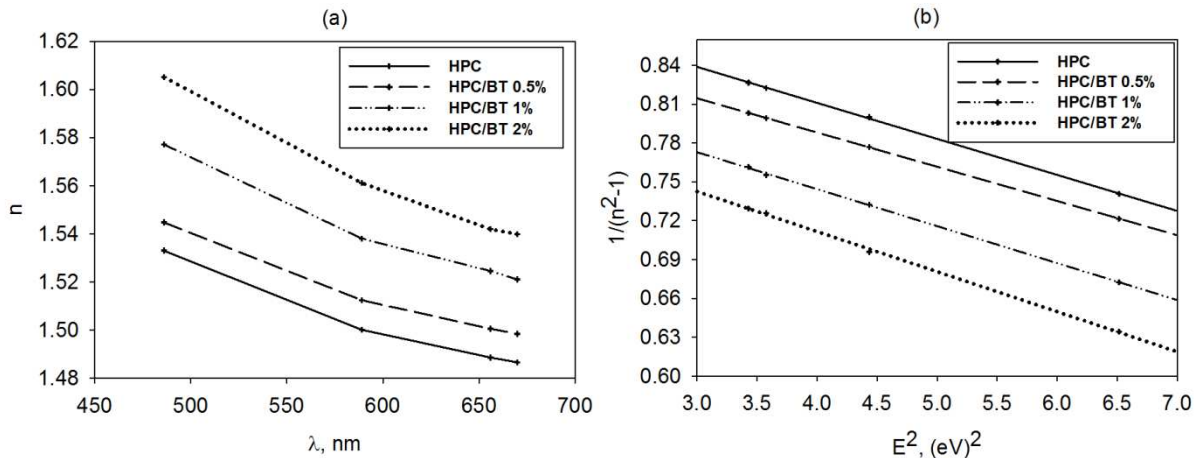
321 **3.4 Refractive index and optical dispersion parameters**

322

323 The refractive index (n) is an optical parameter that is connected to the light speed through the
324 analyzed material. The experimentally determined n values of pristine HPC and HPC/BT composite
325 films as a function of wavelength are displayed in Figure 7a. For all samples the refractive index is
326 decreasing as the light wavelength is gradually increasing. Furthermore, incorporation of BT filler
327 determines the increase of the refractive index comparatively to the pure HPC, namely, at 486 nm, n
328 ranges from 1.533 at 0% BT to 1.605 at 2% BT in the matrix. This kind of enhancement in the
329 refractive index magnitude might be the result of an increase of the composite density, as supported
330 by literature data for polymer composites (Banerjee et al., 2019). Comparable results were reported
331 for other polymer/BT composites, namely the refractive index of HPC/BT samples is smaller than
332 that of poly(arylene ether ketone)/BT (1.65 at 12 wt % BT) (Imai et al., 2010), similar to that of
333 PMMA/BT (1.56 at 10 vol% BT) (Nagao et al., 2011) and higher than that of PMMA/ethylene
334 glycol monovinyl ether/BT (1.53 for BaTiO₃/8EGMVE/10H₂O/5PMMA) (Mimura et al., 2010).
335 Optical dispersion parameters can be obtained by making a close analysis of the refractive index
336 dependence on photon energy. This is described by the Wemple and DiDomenico (WDD) single
337 oscillator model, as shown by equation (4):

338
$$n^2 = 1 + \frac{E_d E_0}{E_0^2 - E^2} \quad (4)$$

339 where E_0 is the average excitation energy for electronic transitions and E_d is the dispersion energy.
340 Figure 7b displays the plots of $1/(n^2 - 1)$ against E^2 for HPC matrix and its BT-containing
341 composites. The values of E_0 and E_d were estimated from the linear fit of the obtained graphs
342 (Figure 7b) and the results are provided in Table 2.



343
344 **FIGURE 7** Refractive index dependence of wavelength (a) and plots of $1/n^2-1$ versus E^2 (b) for
345 neat HPC and HPC/BT composite films

346 The obtained data indicate that the strength of the interband optical transitions, expressed by E_d , are
347 decreasing as the filling level is higher. The average excitation energy E_0 follows the same trend.
348 This behavior was also noticed for polyvinyl alcohol (PVA) filled with BT (Barzic et al., 2020).
349 The oscillator energy varies analogously to the optical band gap energy as the reinforcement level
350 in HPC is higher. However, the values of E_d , E_0 and n_0 for HPC/BT are slightly smaller than those
351 reported for PVA/BT (Barzic et al., 2020).

352

353 **TABLE 2** The values of dispersion energy (E_d), single-oscillator energy (E_0), static refractive index
354 (n_0), linear optical susceptibility ($\chi^{(1)}$), third order optical susceptibility ($\chi^{(3)}$), and nonlinear
355 refractive index (n_{NL}) for HPC and HPC/BT composite films

Sample code	E_d (eV)	E_0 (eV)	n_0	$\chi^{(1)}$	$\chi^{(3)}$ (e.s.u.)	n_{NL} (e.s.u.)
HPC	6.900	6.363	1.444	0.086	$9.43 \cdot 10^{-15}$	$2.46 \cdot 10^{-13}$
HPC/BT 0.5%	6.510	5.818	1.456	0.089	$1.07 \cdot 10^{-14}$	$2.77 \cdot 10^{-13}$
HPC/BT 1%	6.393	5.488	1.471	0.093	$1.26 \cdot 10^{-14}$	$3.23 \cdot 10^{-13}$
HPC/BT 2%	6.225	5.199	1.482	0.095	$1.40 \cdot 10^{-14}$	$3.56 \cdot 10^{-13}$

356

357 The data concerning E_0 and E_d can be utilized to calculate the static refractive index (n_0) at zero
358 photon energy, as revealed by equation (5):

$$359 \quad n_0 = \left(1 + \frac{E_d}{E_0}\right)^{0.5} \quad (5)$$

360 As seen in Table 2, the static refractive index is higher as the inorganic particle amount in HPC
361 matrix is increasing.

362 Optical dispersion parameters lie at the basis for determining nonlinear optical properties (Soliman
363 et al., 2020), namely optical susceptibility and nonlinear refractive index, defined by equations (6-
364 8):

365
$$\chi^{(1)} = \frac{E_d / E_0}{4\pi} \quad (6)$$

366
$$\chi^{(3)} = 6.82 \cdot 10^{-15} \cdot (E_d / E_o)^4 \quad (7)$$

367
$$n_{NL} = \frac{12\pi\chi^{(3)}}{n_0} \quad (8)$$

368 where $\chi^{(1)}$ is the first-order optical susceptibility, $\chi^{(3)}$ is the third-order optical susceptibility and
369 n_{NL} is the nonlinear refractive index.

370 The achieved data for nonlinear optical properties are listed in Table 2. It was found that the
371 insertion of ceramic particles in HPC generates the enhancement of the first and third order optical
372 susceptibility and also of the nonlinear refractive index. The values of $\chi^{(1)}$ and $\chi^{(3)}$ for HPC/BT are
373 smaller comparatively to those of PVA/BT (Barzic et al., 2020), while the nonlinear refractive
374 index of studied samples is higher. These aspects sustain the suitability of the HPC/BT materials for
375 nonlinear optical and photonic devices.

376

377 **3.5 Optical and electrical conductivities**

378

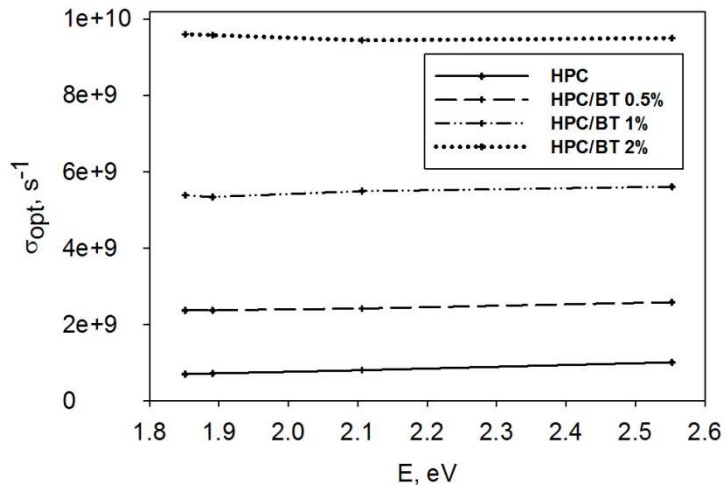
379 The optical conductivity is connected to the refractive index and the optical absorption coefficient at
380 specific wavelengths. For the analyzed composite materials this parameter was evaluated using
381 equation (9):

382
$$\sigma_{opt} = \alpha \cdot n \cdot c / 4\pi \quad (9)$$

383 where σ_{opt} is the optical conductivity and c is the speed of light in empty space.

384 The conductivity at optical frequencies is depicting the material's optical response caused by the
385 travelling of the charge carrier under the action of external electromagnetic waves. Figure 8
386 illustrates the dependence of σ_{opt} with photon energy for the prepared samples. The optical
387 conductivity of the pristine HPC film is not changing very much within energy interval of 1.85-2.55
388 eV. A similar behavior is noticed for the HPC composites containing 0.5-2% BT filler. At 2.1 eV,
389 the optical conductivity increases with an order of magnitude from 10^8 for HPC to 10^9 for HPC/BT
390 2%, which is smaller than that of PVA/BT (Barzic et al., 2020). The enhancement of optical
391 conductivity could be attributed to the formation of new states within the band gap that enable

392 electron crossing between the valence to the nearest state, as observed in the lowering of optical
393 band gap (Table 1).



394

395 **FIGURE 8** Optical conductivity versus photon energy for pristine HPC and HPC/BT composite
396 films

397

398 The electrical conduction properties of HPC and HPC/BT composites were also analyzed at low
399 frequencies. As seen in Figure 9, the measured conductivity (σ) of all examined films is affected by
400 the applied electric field frequency so that it ranges from 10^{-11} S/cm to 10^{-7} S/cm. The conductivity
401 ascended with the increase of frequency. A closer analysis shows that in the lower frequency
402 interval of 1- 10^3 Hz, the variation of σ was gradual, whereas after 10^3 Hz it ranged faster with
403 further augmentation of the frequency. The recorded conductivity and the phase angle (θ) versus
404 frequency are represented in Figures 9a and b. The plateau region of conductivity retrieved at low
405 frequencies connected with the values close to 0° of phase angles are assigned with the DC
406 conductivity (e.g. transport of charge carriers through the polymer matrix). On the other hand, the
407 linear increase of conductivity at high frequencies and phase angle values close to -90° are generally
408 specific to AC conductivity. Such behavior can be explained on the basis of Dyre's random free
409 energy barrier approach (Dyre, 1988). The latter implies that conduction in solids occurs by
410 bouncing of the charge carriers in the localized and highest states in the conduction band. This
411 phenomenon is hasten by applying higher frequencies (Hassan et al., 2018; Tao et al., 2020).

412 On the other hand, the conductivity of HPC material is affected by the addition of ceramic filler.
413 The increase in conduction features is more obvious up to 10^3 Hz in the plateau region of
414 conductivity, whereas after this point the slope of the conductivity curve is slightly increasing with
415 addition of BT particles in the polymer. In other words, the conductivity increase in high frequency
416 zone takes place owing to higher amount of free charges as a result of more polymer-nanoparticle

interactions, combined with the existence of BT inside the polymer, which is known to promote the charge conduction (Morsi et al., 2019). Relatively constant conductivity in low frequency range might be ascribed to polar functional groups from HPC matrix, while for composites, this plateau results from electronic or ionic conductivity. As the filler amount in the system increases, the recorded conductivity increase could be attributed to carrier hopping among the macromolecular chains (Mendes et al., 2012). The level of conductivity at the highest frequency slightly exceeds that reported by Morsi et al for BT incorporated in PEO/CMC at low frequencies (Morsi et al., 2019).

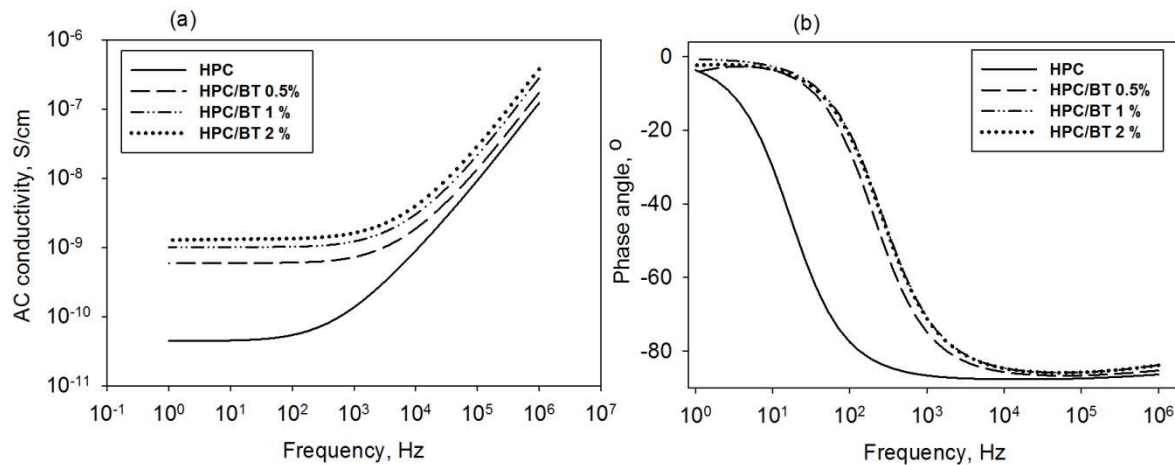


FIGURE 9 Measured conductivity versus frequency for neat HPC and HPC/BT composites

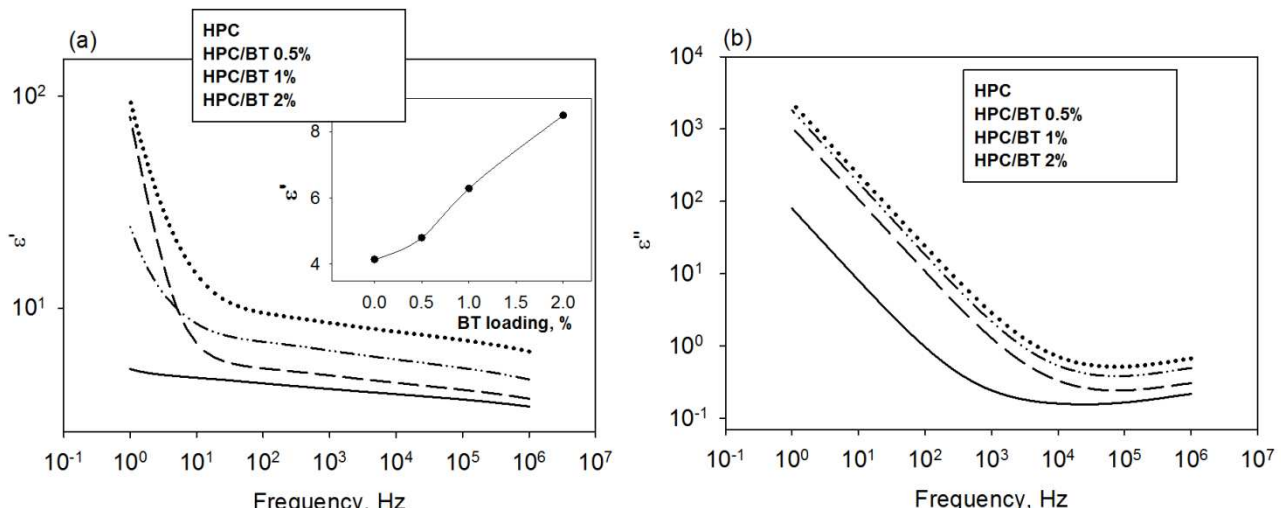
3.6 Dielectric constant and electric energy density

Dielectric spectroscopy was also used to test the dielectric performance of the samples. Figures 10a and b illustrate the double-logarithmic dependence of the real (ϵ') and imaginary (ϵ'') dielectric constant on frequency (f) for neat HPC and HPC/BT composite films. The prepared film of HPC matrix has a permittivity of 3.4-5.2 in the recorded frequency domain. This result is in agreement with that reported by Abdelaziz (Abdelaziz, 2015). However, the obtained ϵ' magnitude for HPC is slightly smaller than that measured by Shinouda et al ($\epsilon' \sim 7.6$) (Shinouda & Abdel Moteleb, 2005) or by Maximean et al ($\epsilon' \sim 19.9$) (Manaila Maximean et al., 2018). The differences could reside from the degree of sample drying, synthesis conditions (influencing the degree of substitution) or polymer processing (film, powder, fiber). It is evident that ϵ' lowers with increasing frequency over the interval of $1-10^6$ Hz. The intensive decline of ϵ' observed at low frequencies for HPC/BT composite samples is specific to the electrode polarization (EP) process (Samet et al., 2015). This effect may appear due to the agglomeration of mobile charges mainly originated from BT source of charge carriers at the contact between sample and the electrodes used for dielectric measurements.

442 As frequency increases, the EP effect is gradually diminished and a slighter reduction of ϵ' is
 443 noticed. The latter behavior reveals the ‘pure’ dipolar activity of the samples. If the frequency is
 444 very high, the dipoles can no longer cope-up with oscillations of the electric field, so the
 445 macromolecules are not orienting along the direction of the applied field (Abdelaziz & Ghannam,
 446 2010). For this reason, as the frequency increases, the dielectric constant gradually becomes smaller
 447 and is almost constant at high frequencies.

448 Generally, for reinforced polymers, the dielectric properties are linked to the filler content and
 449 particle distribution (Morsi et al., 2019). As one may see in Figure 10a, the real part of the dielectric
 450 constant is enhanced upon BT addition within HPC matrix. The permittivity of HPC/BT below 10
 451 Hz were noticed to be high. At 1 kHz, the measured dielectric constant ranges from 4.2 for neat
 452 HPC up to 8.5 for HPC/BT 2% (see the inset graph from Figure 10a).

453 As observed in Figure 10b, the dielectric loss is also higher with further addition of BT particles.
 454 This increase reveals that the charge carrying capacity of the prepared samples is notably larger
 455 with respect to unfilled HPC film. In addition, the high value of dielectric loss noted at low
 456 frequency (under 1 kHz) could be attributable to the mobile charges from the cellulosic matrix. The
 457 linear decrease of ϵ'' retrieved at low frequencies is connected with the σDC plateau region from
 458 Figure 9a and may be attributed to mobile charge carriers from the material.



459
 460 **FIGURE 10** Real (a) and imaginary (b) dielectric constant against frequency for unfilled HPC and
 461 HPC/BT composite films. Inset graph shows variation of real part of permittivity at 1 kHz with BT
 462 loading

463
 464 On the other hand, the low signal from high frequencies is connected with the linear increase of
 465 conductivity and attributed to the loss of energy due to polarization of chemical dipoles. Similar
 466 dielectric behavior was reported for other polymers filled with BT ceramic material (Yao et al.,

467 2018; Ahmed et al., 2018; Beena & Jayanna, 2019). However, at 1 kHz and 2% BT in HPC, the
468 prepared composites have slightly smaller values for ϵ' and ϵ'' than those found in literature for
469 PVA/BT (Beena & Jayanna, 2019), polypyrrole/BT (Ahmed et al., 2018), while the permittivity of
470 our samples is higher than that reported for polypropylene/BT (Yao et al., 2018) and PEO/CMC/BT
471 (Morsi et al., 2019).

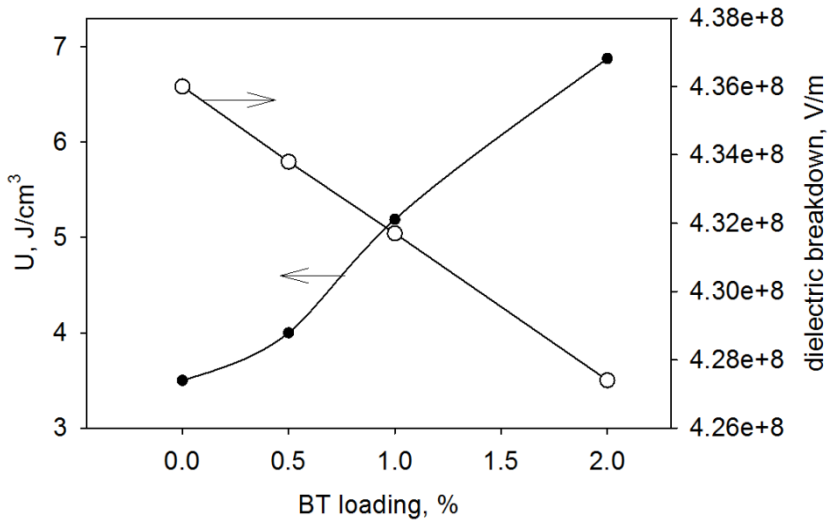
472 Dielectric properties affect the level of energy density within the prepared materials. From practical
473 point of view, this aspect is essential for energy storage applications. The electric energy density
474 (U) for a dielectric is described by equation (10):

475
$$U = \epsilon_0 \epsilon_r E^2 \quad (10)$$

476 where ϵ_0 is permittivity of free space, ϵ_r is the relative permittivity and E is the intensity of the
477 electric field.

478 It is obvious that the discharged energy density of a dielectric can be amended by enhancing either
479 the permittivity of the material or the field intensity. A close analysis of equation (10) indicates that
480 the effect of field's intensity has a greater impact on U magnitude because it appears in relation in
481 the second order. The highest energy density is obtained at the point of material's breakdown
482 strength. Reinforced polymers have received special attention owing to the possibility to control the
483 electrical characteristics in regard to the properties of single phase materials (Huang & Jiang, 2015),
484 whilst having the opportunity for upgrading the mechanical properties, in terms of mechanical
485 flexibility or toughness. Ferroelectric particles, such as BT, are ideal for improving the dielectric
486 performance of the polymers owing to their high permittivity.

487 According to Stark and Garton model (Stark & Garton, 1955), the dielectric breakdown strength
488 ranges proportionally with yields stress and is the reverse of the materials permittivity. The yield
489 stress for HPC was reported to be 3.5 MPa (Borges et al., 2004). Based on these aspects, for HPC
490 matrix the breakdown strength is $4.367 \cdot 10^8$ V/m. Literature shows that addition of BT particles in a
491 polymer determines lowering of the breakdown strength (Dou et al., 2009; Yu et al., 2013).
492 Knowing that the dielectric breakdown of BT is $38 \cdot 10^5$ V/m (Branwood et al., 1962), the
493 corresponding values for the studied composites were estimated and depicted in Figure 11. In order
494 to determine the maximum values of the electric energy density, this parameter was assessed at
495 electric field intensities corresponding to the breakdown strength.



496

497 **FIGURE 11** Electric energy density for neat HPC and HPC/BT composites as a function of BT
498 loading

499

500 Figure 11 shows the variation of electric energy density with BT amount introduced in HPC.
501 Similar values to our results were reported for polyimide/reduced BT and poly(vinyl alcohol)/BT
502 composites (Yue et al., 2019; Liu et al., 2020). The increase of U parameter with further addition of
503 ceramic inclusions in the cellulose derivative matrix is a promising indicative for energy storage
504 applications.

505

506 **4. CONCLUSIONS**

507

508 New polymer composites were fabricated by embedding ceramic particles in a cellulose derivative
509 matrix. Addition of BT filler favor production of supplementary localized energy states in the
510 forbidden energy zone, thus reducing transparency of films and direct band gap energy from 6.12
511 eV for neat HPC to 5.74 eV for HPC/BT 2%. Optical micrographs indicate a good dispersion of
512 ceramic particles within HPC material owing to ultrasonication of the samples. Also, the presence
513 of BT inclusions increases polarizability and implicitly the refractive index from 1.53 to 1.61 at 489
514 nm. Moreover, optical and AC conductivity of HPC is improved after reinforcement, together with
515 dielectric constant that increases from 4.2 for pristine HPC up to 8.5 for HPC/BT 2%. This is
516 reflected in a higher electric energy density and recommends the studied materials for energy
517 storage applications.

518

519

520

521 **Declarations**

523 **Funding:** Not applicable.

525 **Conflicts of interest/Competing interests:** The authors declare no conflict of interests.
526
527 **Ethics approval:** Not applicable.

529 **Consent to participate:** All authors consent to participate at the research included in this work and
530 approve the manuscript submission.

532 **Consent for publication:** All authors agree with article publication.

534 **REFERENCES**

536 Abdel-Halim, E. S., Alanazi, H. H., & Al-Deyab, S. S. (2015). Utilization of olive tree branch
537 cellulose in synthesis of hydroxypropyl carboxymethyl cellulose. *Carbohydrate Polymers*, 127,
538 124-134.

539 Abdelaziz, M., & Ghannam, M. M. (2010). Influence of titanium chloride addition on the optical
540 and dielectric properties of PVA films. *Physica B: Condensed Matter*, 405, 958-964.

541 Abdelaziz, M. (2015). Effect of Sm³⁺ substitution on structural, optical and dielectric properties of
542 hydroxypropyl cellulose films. *Journal of Materials Science: Materials in Electronics*, 26(11),
543 8688-8697.

544 Ahmed, K., Kanwal, F., Ramay, S. M., Atiq, S., Rehman, R., Ali, S. M., & Alzayed, N. S. (2018).
545 Synthesis and Characterization of BaTiO₃/Polypyrrole Composites with Exceptional Dielectric
546 Behaviour. *Polymers*, 10, 1273.

547 Ali, A. F., Hassan, M. L., Ward, A. A., & El-Giar, E. M. (2017). Processing, dynamic mechanical
548 thermal analysis, and dielectric properties of barium titanate/cellulosic polymer nanocomposites.
549 *Polymer Composites*, 38, 893-907.

550 Banerjee, M., Jain, A., & Mukherjee, G. S. (2019). Microstructural and optical properties of
551 polyvinyl alcohol/manganese chloride composite film. *Polymer Composites*, 40, E765-E775.

552 Barzic, A. I., Soroceanu, M., Rotaru, R., Harabagiu, V., & Ciobanu, R. C. (2020). Optical
553 Dispersion Characteristics of Polyvinyl Alcohol Reinforced with a Nanoceramic Filler. *Materiale
554 Plastice (Mater. Plast.)*, 57, 1-7.

- 555 Beena, P., & Jayanna, H. S. (2019). Dielectric studies and AC conductivity of piezoelectric barium
556 titanate ceramic polymer composites. *Polymers and Polymer Composites*, 27, 619-625.
- 557 Borges, J. P., Godinho, M. H., & Martins, A. F. (2004). Tensile Properties of Cellulose Fiber
558 Reinforced Hydroxypropylcellulose Films. *Polymer Composites*, 25, 102-110.
- 559 Branwood, A., Hughes, O. H., Hurd, J. D., & Tredgold, R. H. (1962). Dielectric breakdown in
560 barium titanate. *Proc Phys Soc*, 79, 1161.
- 561 Choudhary, S., & Sengwa, R. J. (2018). ZnO nanoparticles dispersed PVA–PVP blend matrix based
562 high performance flexible nanodielectrics for multifunctional microelectronic devices. *Current
563 Applied Physics*, 18, 1041-1058.
- 564 Dou, X., Liu, X., Zhang, Y., Feng, H., Chen, J.-F., & Du, S. (2009). Improved dielectric strength of
565 barium titanate-polyvinylidene fluoride nanocomposite. *Applied Physics Letters*, 95(13), 132904.
- 566 Dyre, J. C. (1988). The random free-energy barrier model for ac conduction in disordered solids.
567 *Journal of Applied Physics*, 64, 2456.
- 568 Gao, L., Liu, Q., Gao, Z., & Lin, Y. (2008). Preparation and characterization of
569 polyimide/silica-barium titanate nanocomposites. *Polymer Composites*, 29, 1160-1164.
- 570 Goyal, R. K., Katkade, S. S., & Mule, D. M. (2013). Dielectric, mechanical and thermal properties
571 of polymer/BaTiO₃ composites for embedded capacitor. *Composites Part B: Engineering*, 44, 128-
572 132.
- 573 Gu, L., Li, T., Xu, Y., Sun, C., Yang, Z., Zhu, D., & Chen, D. (2019). Effects of the particle size of
574 BaTiO₃ fillers on fabrication and dielectric properties of BaTiO₃/polymer/Al films for capacitor
575 energy-storage application. *Materials*, 12, 439.
- 576 Hassan, M. L., Ali, A. F., Salama, A. H., & Abdel-Karim, A. M. (2018). Novel cellulose
577 nanofibers/barium titanate nanoparticles nanocomposites and their electrical properties. *Journal of
578 Physical Organic Chemistry*, 32, e3897.
- 579 Hua, Z., Shi, X., & Chen, Y. (2019). Preparation, structure, and property of highly filled polyamide
580 11/BaTiO₃ piezoelectric composites prepared through solid-state mechanochemical method.
581 *Polymer Composites*, 40, E-177-E-185.
- 582 Huang X., & Jiang P. (2015). Core-Shell Structured High-k Polymer Nanocomposites for Energy
583 Storage and Dielectric Applications. *Advanced Materials*, 27, 546-554.
- 584 Huang, X., Zeng, J., Yu, H., Wei, X., Pu, L., & Liu, J. (2020). NiNb₂O₆-BaTiO₃/poly(arylene ether
585 nitriles) composite film dielectrics with excellent flexibility and high permittivity for organic film
586 capacitors. *Polymer Composites*, 41, 94-101.

- 587 Imai, Y., Terahara, A., Hakuta, Y., Matsui, K., Hayashi, H., & Ueno, N. (2010). Synthesis and
588 characterization of high refractiveindex nanoparticle/poly(arylene ether ketone) nanocomposites.
589 *Polymer Journal*, 42,179-184.
- 590 Joshi, G., Rana, V., Naithani, S., Varshney, V. K., Sharma, A., & Rawata, J. S. (2019). Chemical
591 modification of waste paper: An optimization towards hydroxypropyl cellulose synthesis.
592 *Carbohydrate Polymers*, 223, 115082.
- 593 Kesavan, K., Rajendran, S., & Mathew, C. M. (2015). Influence of Barium Titanate on poly(vinyl
594 pyrrolidone)-based composite polymer blend electrolytes for lithium battery applications. *Polymer*
595 *Composites*, 36, 302-311.
- 596 Kobayashi, Y., Kurosawa, A., Nagao, D., & Konno, M. (2010). Fabrication of Barium Titanate
597 Nanoparticles-EpoxyResin Composite Films and Their Dielectric Properties. *Polymer Composites*,
598 31, 1179-1183.
- 599 Liu, G., Li, Y., Guo, B., Tang, M., Li, Q., Dong, J., Yu, L., Yu, K., Yan, Y., Wang, D., Zhang, L.,
600 Zhang, H., He, Z., & Jin, L. (2020). Ultrahigh dielectric breakdown strength and excellent energy
601 storage performance in lead-free barium titanate-based relaxor ferroelectric ceramics via a
602 combined strategy of composition modification, viscous, polymer processing, and liquid-phase
603 sintering. *Chemical Engineering Journal*, 398, 125625.
- 604 Lombardi, M., Guerriero, A., Kortaberria, G., Mondragon, I., Sangermano, M., & Montanaro, L.
605 (2011). Effect of the ceramic filler features on the properties of photopolymerized BaTiO₃-acrylic
606 composites. *Polymer Composites*, 32, 1304-1312.
- 607 Malathi, M., Tamilarasan, K., & Ganesan, V. (2015). Role of ceramic reinforcement in composite
608 polymer electrolyte. *Polymer Composites*, 36, 42-46.
- 609 Manaila Maximean, D., Danila, O., Ganea, C. P., & Almeida, P. L. (2018). Filling in the voids of
610 electrospun hydroxypropyl cellulose network: Dielectric investigations. *The European Physical*
611 *Journal Plus*, 133, 159.
- 612 Mendes, S. F., Costa, C. M., Caparros, C., Sencadas, V., & Lanceros-Méndez, S. (2012). Effect of
613 filler size and concentration on the structure and properties of poly (vinylidene fluoride)/BaTiO₃
614 nanocomposites. *Journal of Materials Science*, 47, 1378-1388.
- 615 Mimura, K., Hiramatsu, K., Moriya, M., Sakamoto, W., Kawado, S., Uesu, Y., & Yogo, T. (2010).
616 Optical properties of transparent barium titanate nanoparticle/polymer hybrid synthesized from
617 metal alkoxides. *Journal of Nanoparticle Research*, 12, 1933-1943.
- 618 Mohd Ishak, N. A., Khalil, I., Abdullah, F. Z., & Julkapli, N. M. (2020). A correlation on
619 ultrasonication with nanocrystalline cellulose characteristics. *Carbohydrate Polymers*, 246, 116553.

- 620 Morsi, M. A., Abdelaziz, M., Oraby, A. H., & Mokhles, I. (2019). Structural, optical, thermal, and
621 dielectric properties of polyethylene oxide/carboxymethyl cellulose blend filled with barium
622 titanate. *Journal of Physics and Chemistry of Solids*, 125, 103-114.
- 623 Nagao, D., Kinoshita, T., Watanabe, A., & Konno, M. (2011). Fabrication of highly refractive,
624 transparent BaTiO₃/poly(methyl methacrylate) composite films with high permittivities. *Polymer*
625 *International*, 60, 1180-1184.
- 626 Nishio, Y., & Takahashi, T. (1984). Morphological study of hydroxypropyl cellulose films prepared
627 from thermotropic melt under shear. *Journal of Macromolecular Science, Part B: Physics*, 23(4-6),
628 483-495.
- 629 Olmos, D., Montero, F., Gonzalez-Gaitano, G., & Gonzalez-Benito, J. (2013). Structure and
630 morphology of composites based on polyvinylidene fluoride filled with BaTiO₃ submicrometer
631 particles: Effect of processing and filler content. *Polymer Composites*, 34, 2094-2104.
- 632 Pant, H. C., Patra, M. K., Verma, A., Vadera, S. R., & Kumar, N. (2006). Study of the dielectric
633 properties of barium titanate-polymer composites. *Acta Materialia*, 54, 3163-3169.
- 634 Petrovsky, V., Petrovsky, T., Kamlapurkar, S., & Dogan, F. (2008). Dielectric Constant of Barium
635 Titanate Powders Near Curie Temperature. *Journal of the American Ceramic Society*, 91, 3590.
- 636 Rotaru, R., Peptu, C., & Harabagiu, V. (2016). Viscose-barium titanate composite for
637 electromagnetic shielding. *Cellulose Chemistry and Technology*, 50 (5-6), 621-628.
- 638 Rotaru, R., Peptu, C., Samoilă, P., & Harabagiu, V. (2017). Preparation of ferroelectric barium
639 titanate through an energy effective solid state ultrasound assisted method. *Journal of the American*
640 *Ceramic Society*, 100, 4511-4518.
- 641 Samet, M., Levchenko, V., Boiteux, G., Seytre, G., Kallel, A., & Serghei, A. (2015). Electrode
642 polarization vs. Maxwell-Wagner-Sillars interfacial polarization in dielectric spectra of materials:
643 Characteristic frequencies, and scaling laws. *The Journal of Chemical Physics*, 142, 194703.
- 644 Sen, F., Basturk, E., Karadoğan, B., Madakbaş, S., & Kahraman, M. V. (2016). Effect of barium
645 titanate on the thermal, morphology, surface, and mechanical properties of the thermoplastic
646 polyurethane/barium titanate composites. *Polymer-Plastics Technology and Engineering*, 55, 1325-
647 1331.
- 648 Sengwa, R. J., Choudhary, S., & Dhatarwal, P. (2019). Nonlinear optical and dielectric properties of
649 TiO₂ nanoparticles incorporated PEO/PVP blend matrix based multifunctional polymer
650 nanocomposites. *Journal of Materials Science - Materials in Electronics*, 30, 12275-13294.
- 651 Sharma, R., Varshney, V. K., Chauhan, G. S., Naithani, S., & Soni P. L. (2009).
652 Hydroxypropylation of Cellulose Isolated from Bamboo(*Dendrocalamus strictus*) with Respect to

- 653 HydroxypropoxylContent and Rheological Behavior of the HydroxypropylCellulose. *Journal of*
654 *Applied Polymer Science*, 113, 2450-2455.
- 655 Shinouda, H. G., & Abdel Moteeb, M. M. (2005). Dielectric Spectroscopy and Relaxation
656 Phenomena of Moistened and Dry Polysaccharides. *Journal of Applied Polymer Science*, 98, 571-
657 582.
- 658 Silva, S. M. C., Pinto, F. V., Antunes, F. E., Miguel, M. G., Sousa, J. J. S., & Pais, A. A. C. C.
659 (2008). Aggregation and gelation in hydroxypropylmethyl cellulose aqueous solutions. *Journal of*
660 *Colloid and Interface Science*, 327, 333-340.
- 661 Soliman, T. S., Vshivkov, S. A., & Elkalashy, Sh. I. (2020). Structural, linear and nonlinear optical
662 properties of Ni nanoparticles – Polyvinyl alcohol nanocomposite films for optoelectronic
663 applications Optical Materials. *Optical Materials*, 107, 110037.
- 664 Stark, K., & Garton, C. (1955). Electric Strength of Irradiated Polythene, *Nature*, 176, 1225-1226.
- 665 Takenaka, T. (2013). Lead-Free Piezoelectric Ceramics. In Handbook of Advanced Ceramics
666 (Second Edition), Materials, Applications, Processing, and Properties (pp. 429-446). Academic
667 Press.
- 668 Tao, J., Cao, S.-an, Feng, R., & Deng, Y. (2020). High dielectric thin films based on barium titanate
669 and cellulose nanofibrils. *RSC Advances*, 10, 5758-5765.
- 670 Tauc, J. (1967). The optical properties of solids. *Physics Today*, 20, 105.
- 671 Valiyaneerilakkal, U., Singh, A., Subash, C. K., Singh, K., Abbas, S. M., & Varghese, S. (2015).
672 Preparation and characterization of poly(vinylidene fluoride-trifluoroethylene)/barium titanate
673 polymer nanocomposite for ferroelectric applications. *Polymer Composites*, 38, 1655-1661.
- 674 Vanderghem, C., Jacquet, N., Danthine, S., Blecker, C., & Paquot, M. (2012). Effect of
675 physicochemical characteristics of cellulosic substrates on enzymatic hydrolysis by means of a
676 multi-stage process for cellobiose production. *Applied Biochemistry and Biotechnology*, 166, 1423-
677 1432.
- 678 Xu, W., Ding, Y., Jiang, S., Ye, W., Liao, X., & Hou, H. (2016). High permittivity nanocomposites
679 fabricated from electrospun polyimide/BaTiO₃ hybrid nanofibers. *Polymer Composites*, 37, 794-
680 801.
- 681 Yang, Y., Pan, H., Xie, G., Jiang, Y., Chen, C., Su, Y., Wang, Y., & Tai, H. (2020). Flexible
682 piezoelectric pressure sensor based on polydopamine-modified BaTiO₃/PVDF composite film for
683 human motion monitoring. *Sensors and Actuators A: Physical*, 301, 111789.
- 684 Yao, J., Hu, L., Zhou, M., You, F., Jiang, X., Gao, L., Wang, Q., Sun, Z., & Wang J. (2018).
685 Synergistic Enhancement of Thermal Conductivity and Dielectric Properties in Al₂O₃/BaTiO₃/PP
686 Composites. *Materials*, 11(9), 1536.

- 687 Yogamalar, N. R., Kalpana, S., Senthil, V., & Chithambararaj, A. (2018). In Multifunctional
688 Photocatalytic Materials for Energy (Eds.). Ferroelectrics for photocatalysis (pp. 307-324).
689 Woodhead Publishing.
- 690 Yu, K., Niu, Y., Xiang, F., Zhou, Y., Bai, Y., & Wang, H. (2013). Enhanced electric breakdown
691 strength and high energy density of barium titanate filled polymer nanocomposites. *Journal of*
692 *Applied Physics*, 114, 174107.
- 693 Yue, S., Wan, B., Liu, Y., & Zhang, Q. (2019). Significantly enhanced dielectric constant and
694 energy storage properties in polyimide/reduced BaTiO₃ composite films with excellent thermal
695 stability. *RSC Advances*, 9, 7706-7717.
- 696 Zhang, C., Yin, Y., Yang, Q., Shi, Z., Hu, G. H., & Xiong C. (2019). Flexible Cellulose/BaTiO₃
697 Nanocomposites with High Energy Density for Film Dielectric Capacitor. *ACS Sustainable*
698 *Chemistry & Engineering*, 7, 10641-10648.

Figures

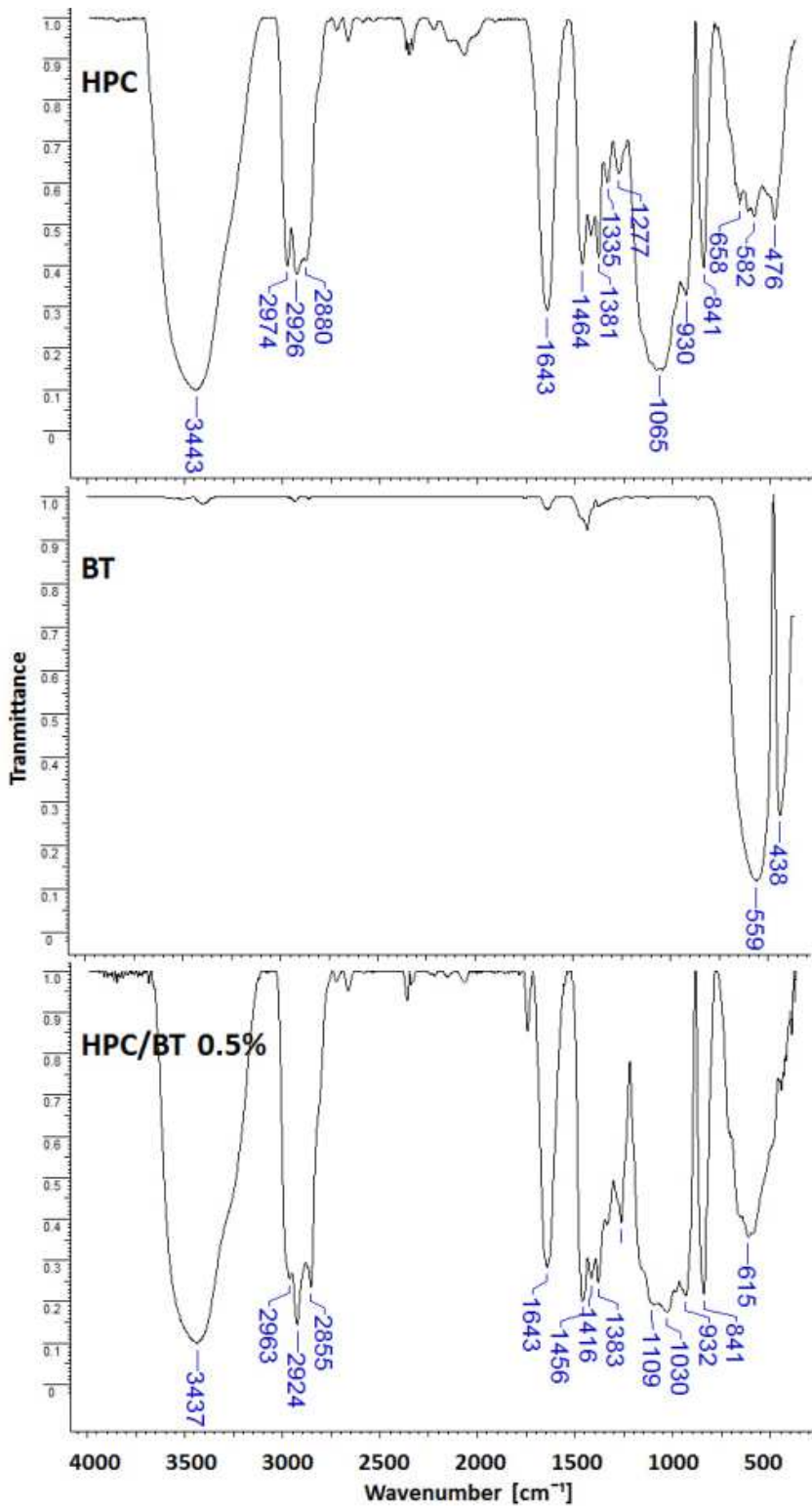


Figure 1

FTIR spectra of HPC film, BT powder, and HPC/BT 05% composite films

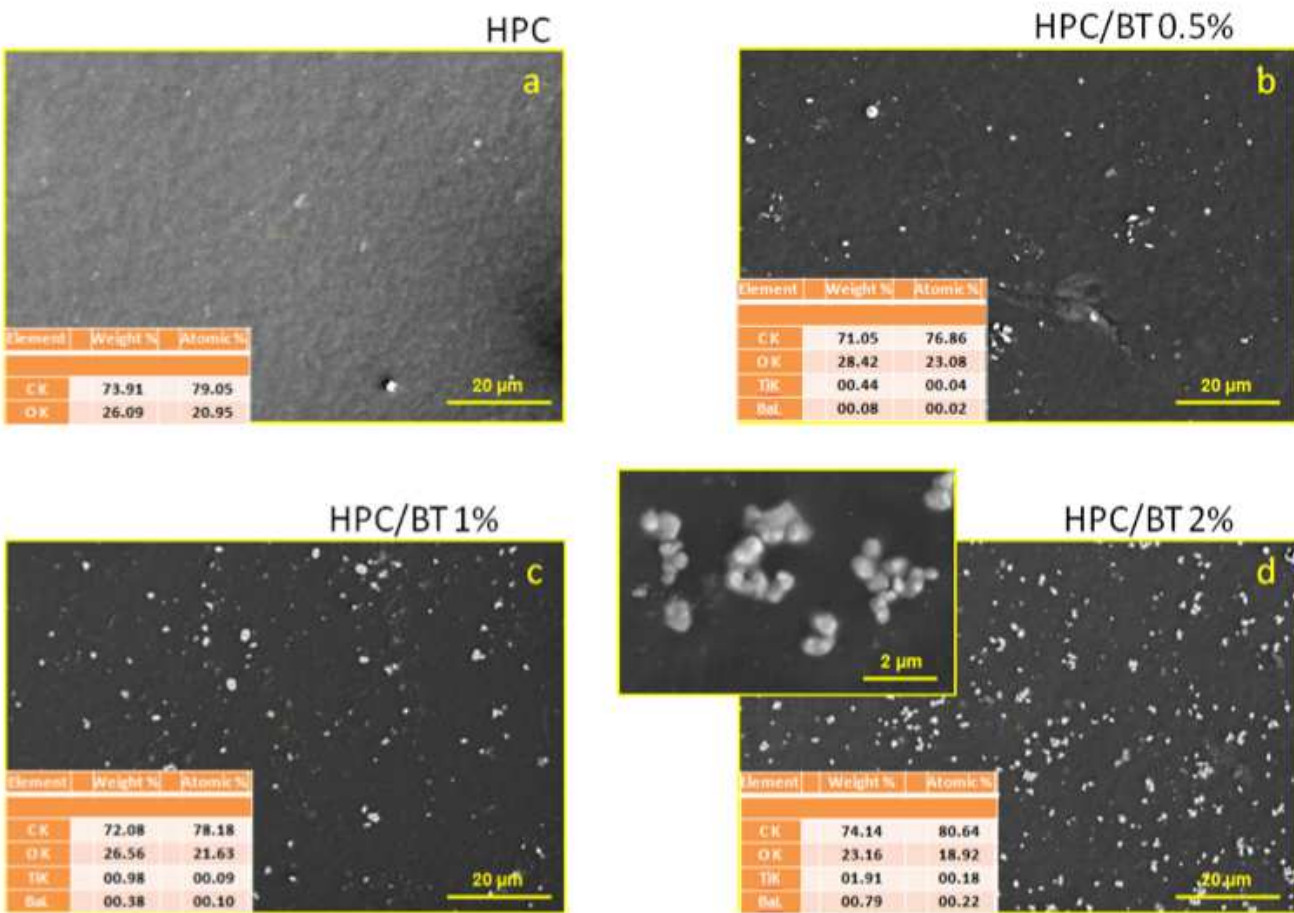


Figure 2

SEM micrographs of the surface of HPC and HPC/BT composites: (a) HPC, (b) HPC/BT 0.5%, (c) HPC/BT 1% and (d) HPC/BT 2%

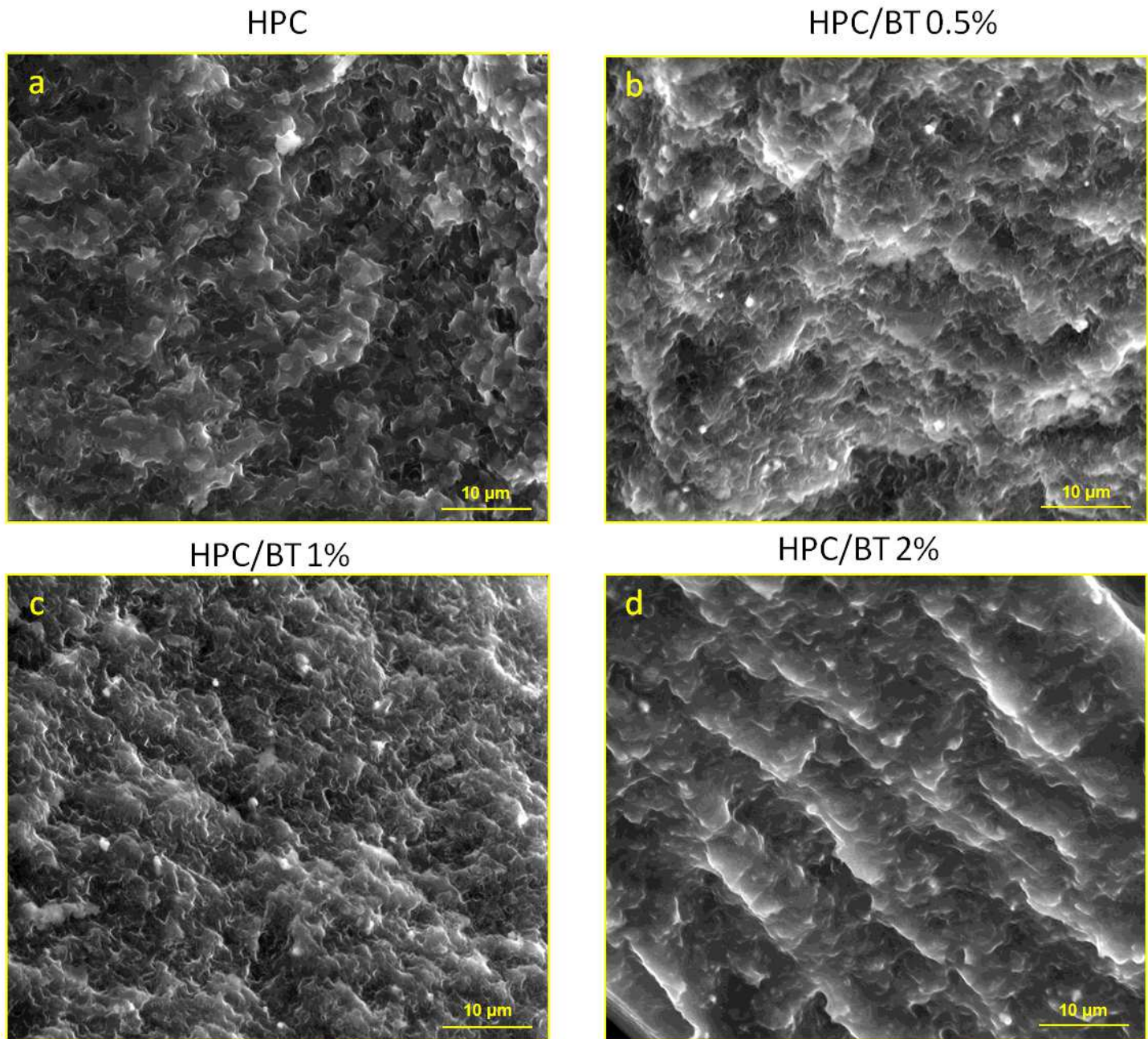


Figure 3

SEM micrographs: Cross-sections of HPC and HPC/BT composites films: (a) HPC, (b) HPC/BT 0.5%, (c) HPC/BT 1% and (d) HPC/BT 2%

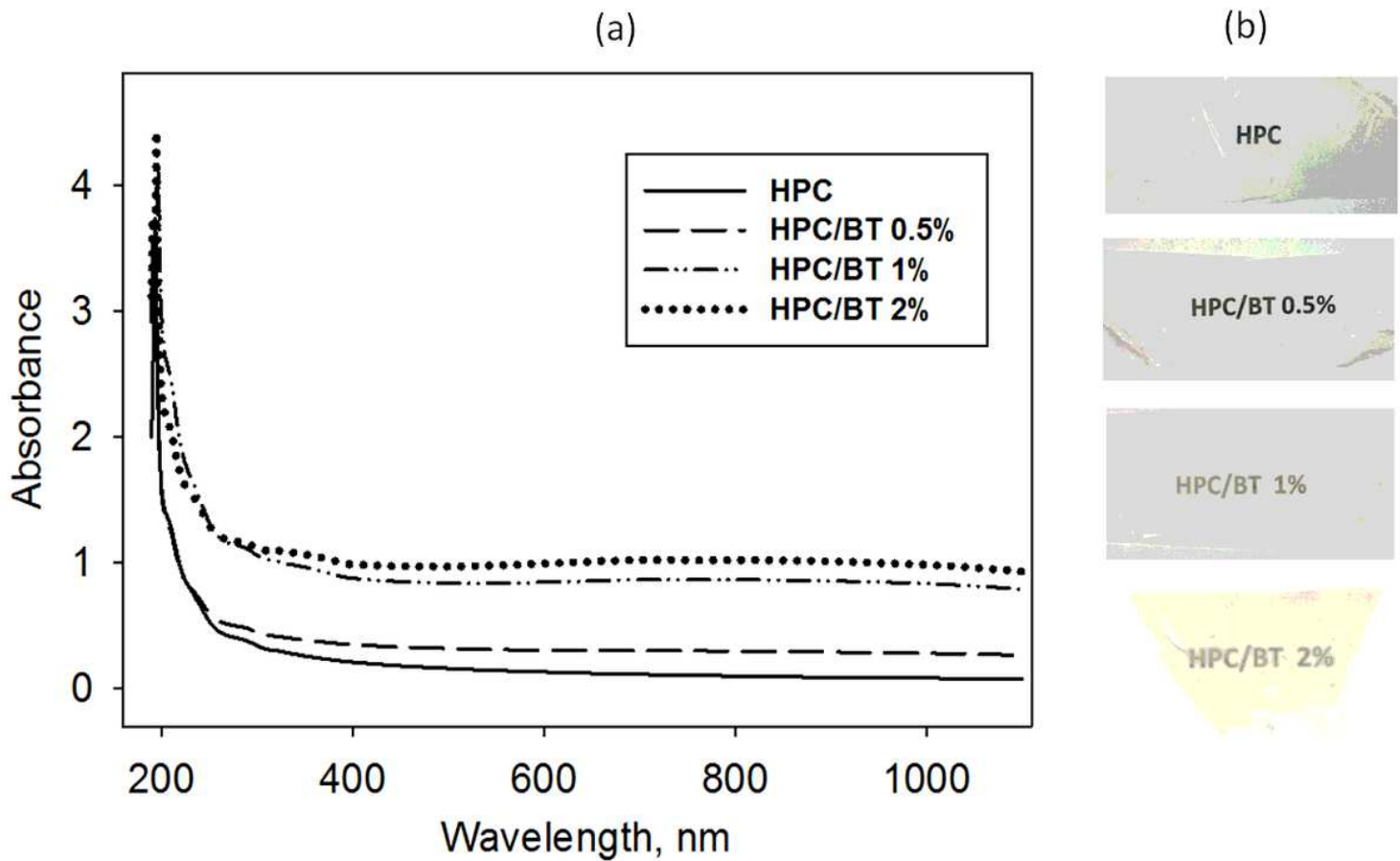


Figure 4

UV-VIS-NIR spectrum of the neat HPC and HPC/BT composite films (a) and the pictures of analyzed samples (b)

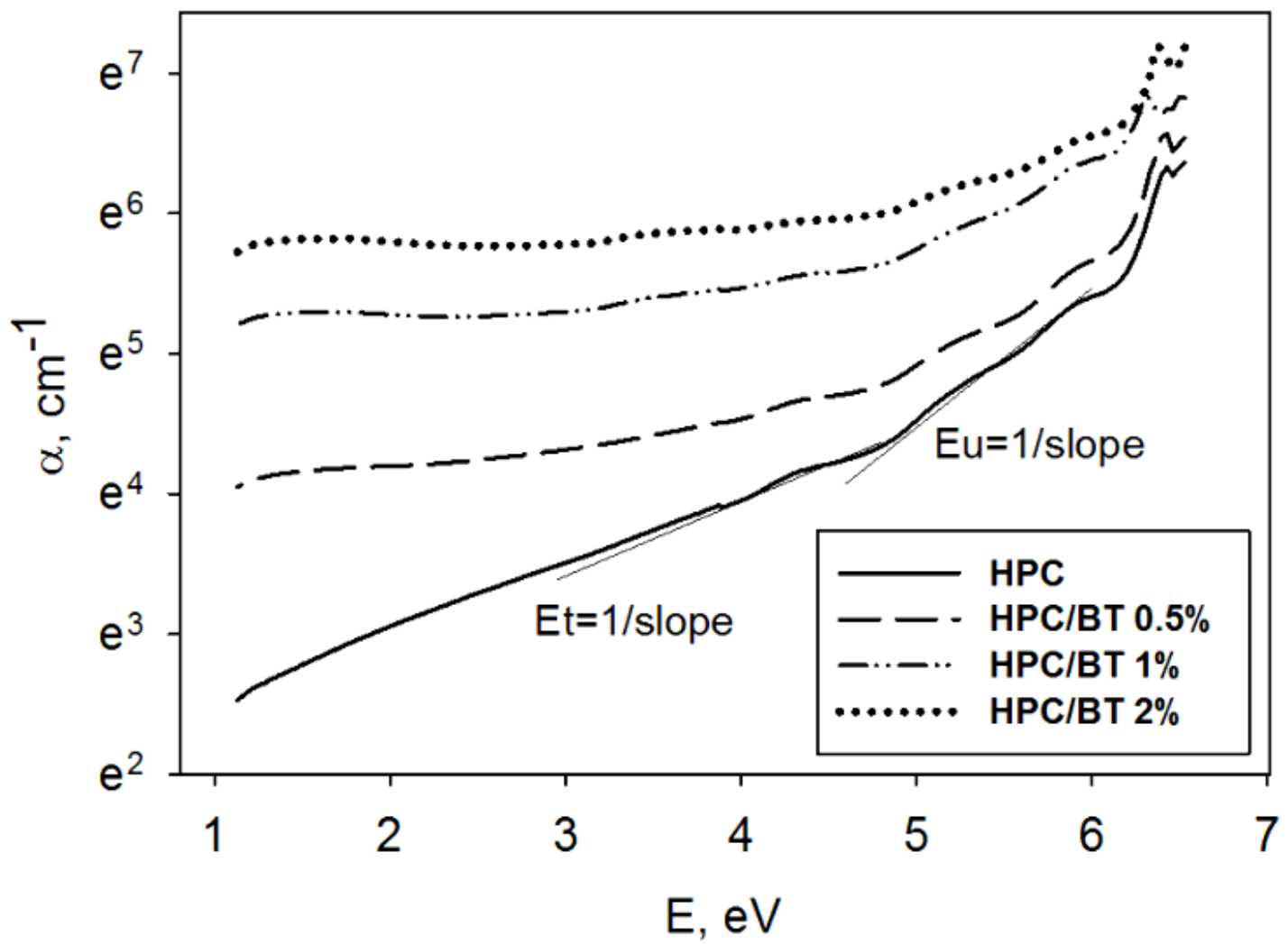


Figure 5

Optical absorption coefficient versus photon energy for unfilled HPC and HPC/BT composite films

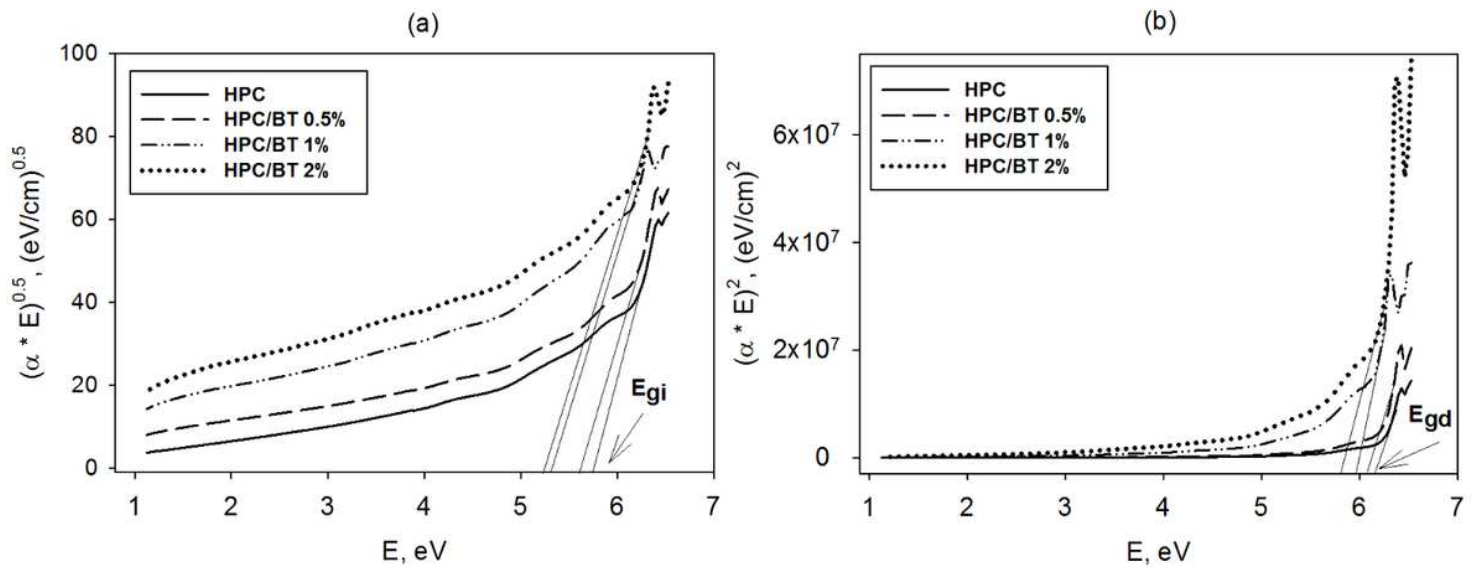


Figure 6

Plots of $(\alpha * E)^{0.5}$ versus E (a) and $(\alpha * E)^2$ versus E (b) for pristine HPC and HPC/BT composite films

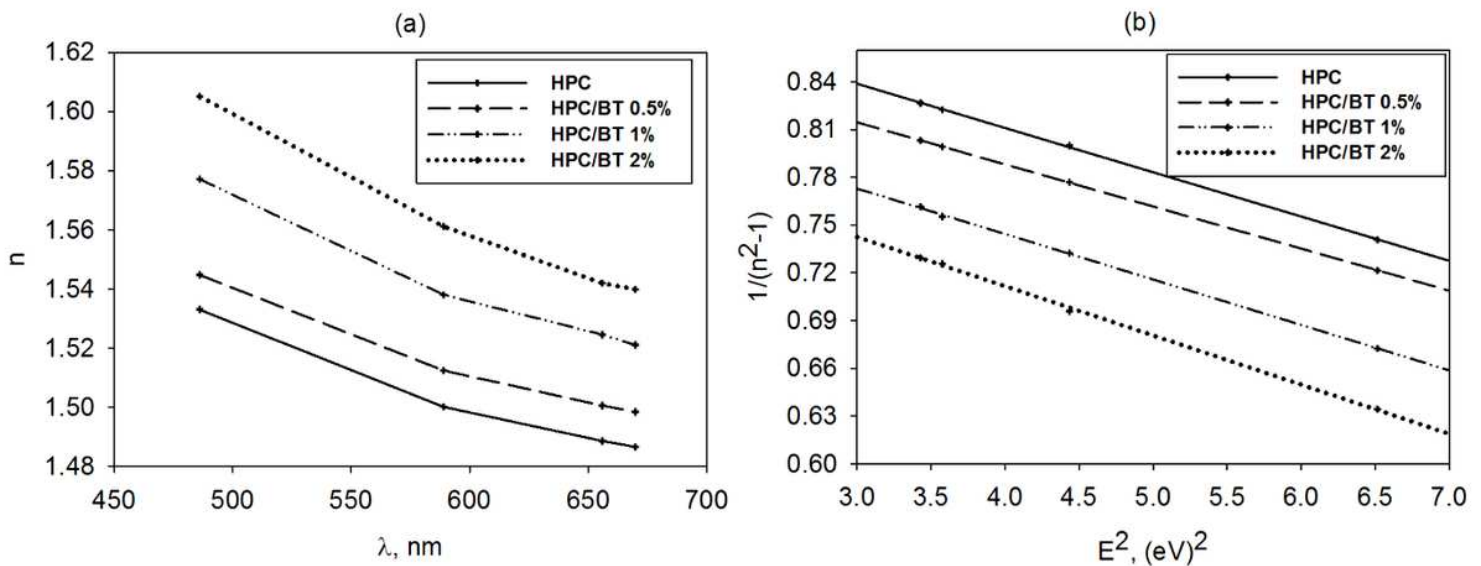


Figure 7

Refractive index dependence of wavelength (a) and plots of $1/n^2-1$ versus E^2 (b) for neat HPC and HPC/BT composite films

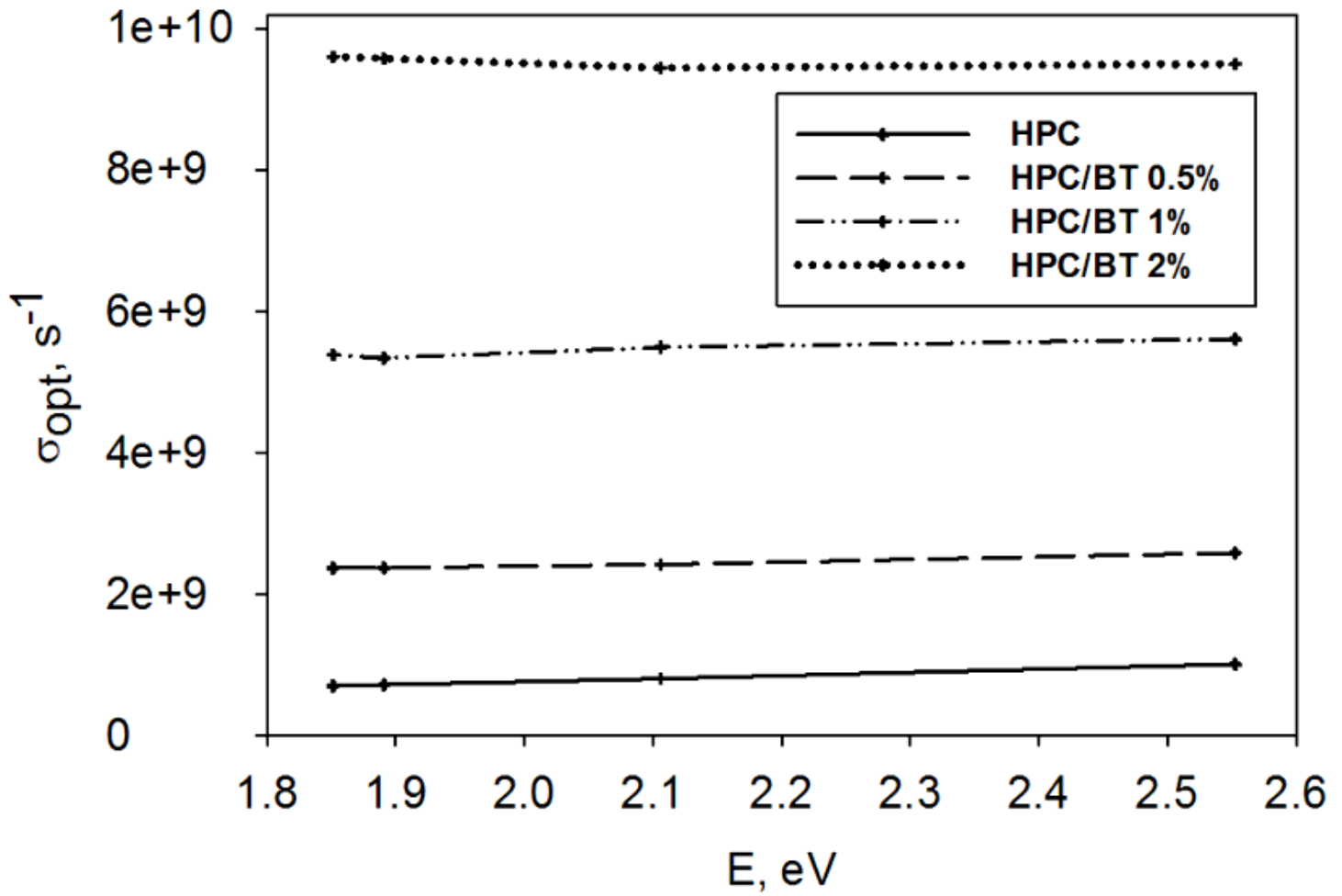


Figure 8

Optical conductivity versus photon energy for pristine HPC and HPC/BT composite films

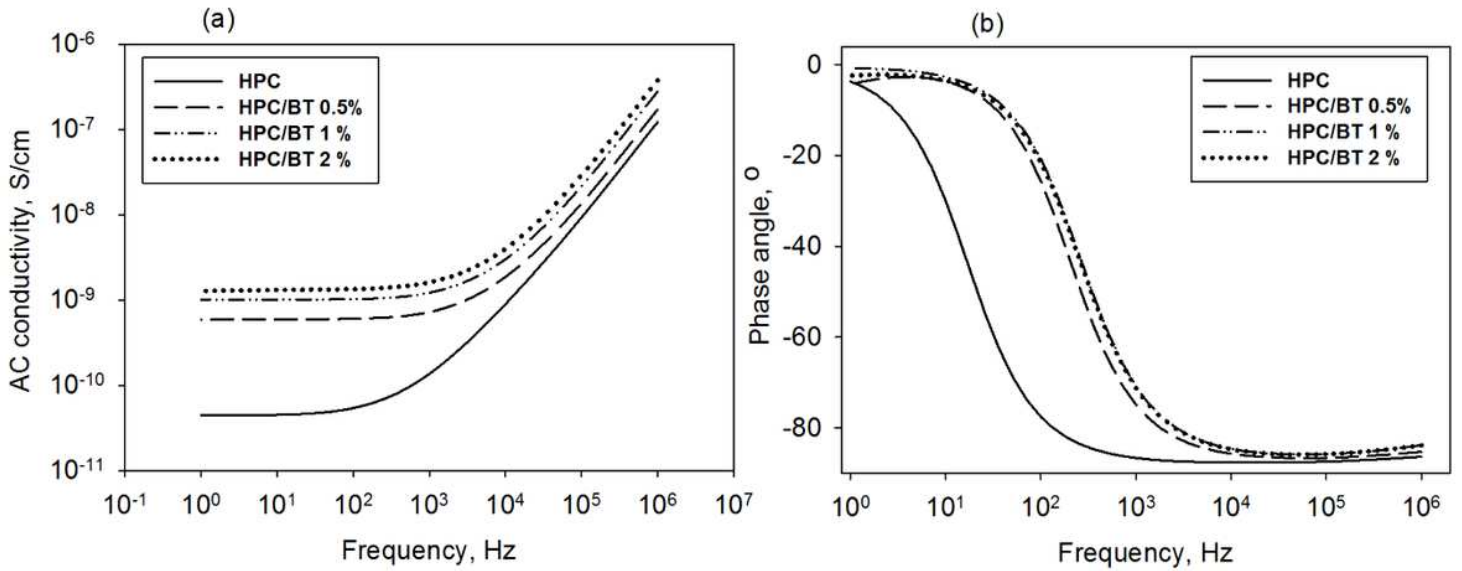


Figure 9

Measured conductivity versus frequency for neat HPC and HPC/BT composites

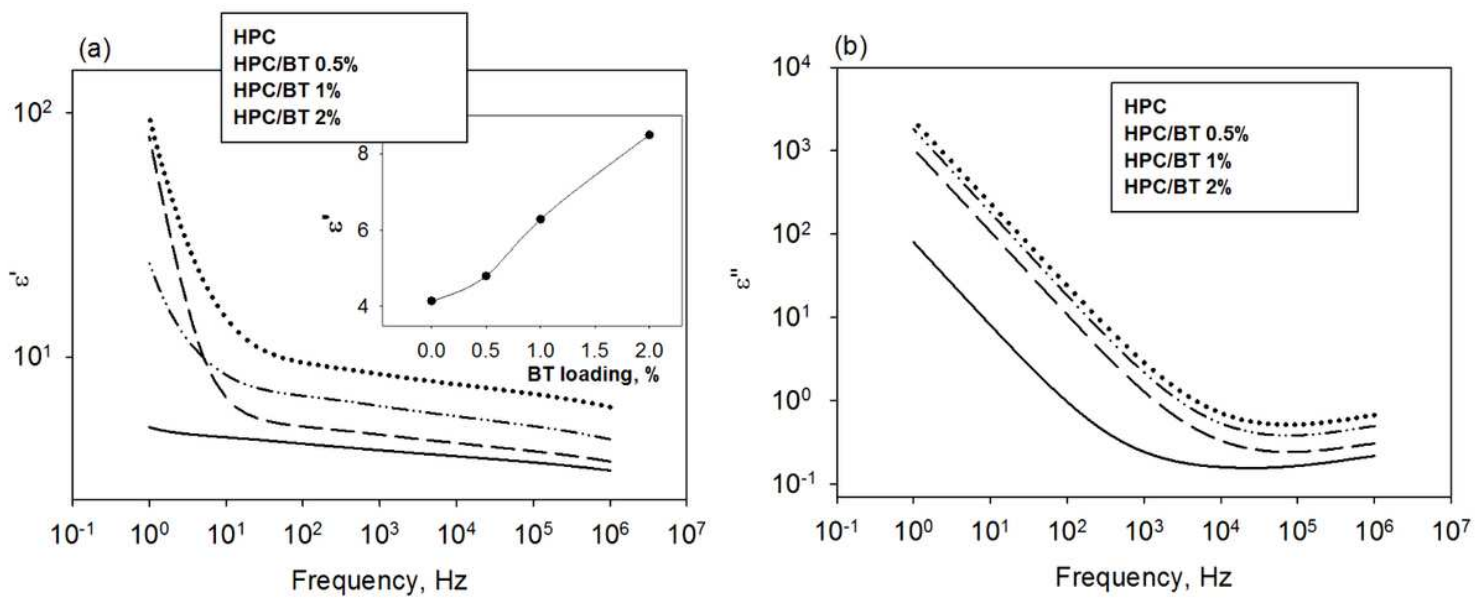


Figure 10

Real (a) and imaginary (b) dielectric constant against frequency for unfilled HPC and HPC/BT composite films. Inset graph shows variation of real part of permittivity at 1 kHz with BT loading

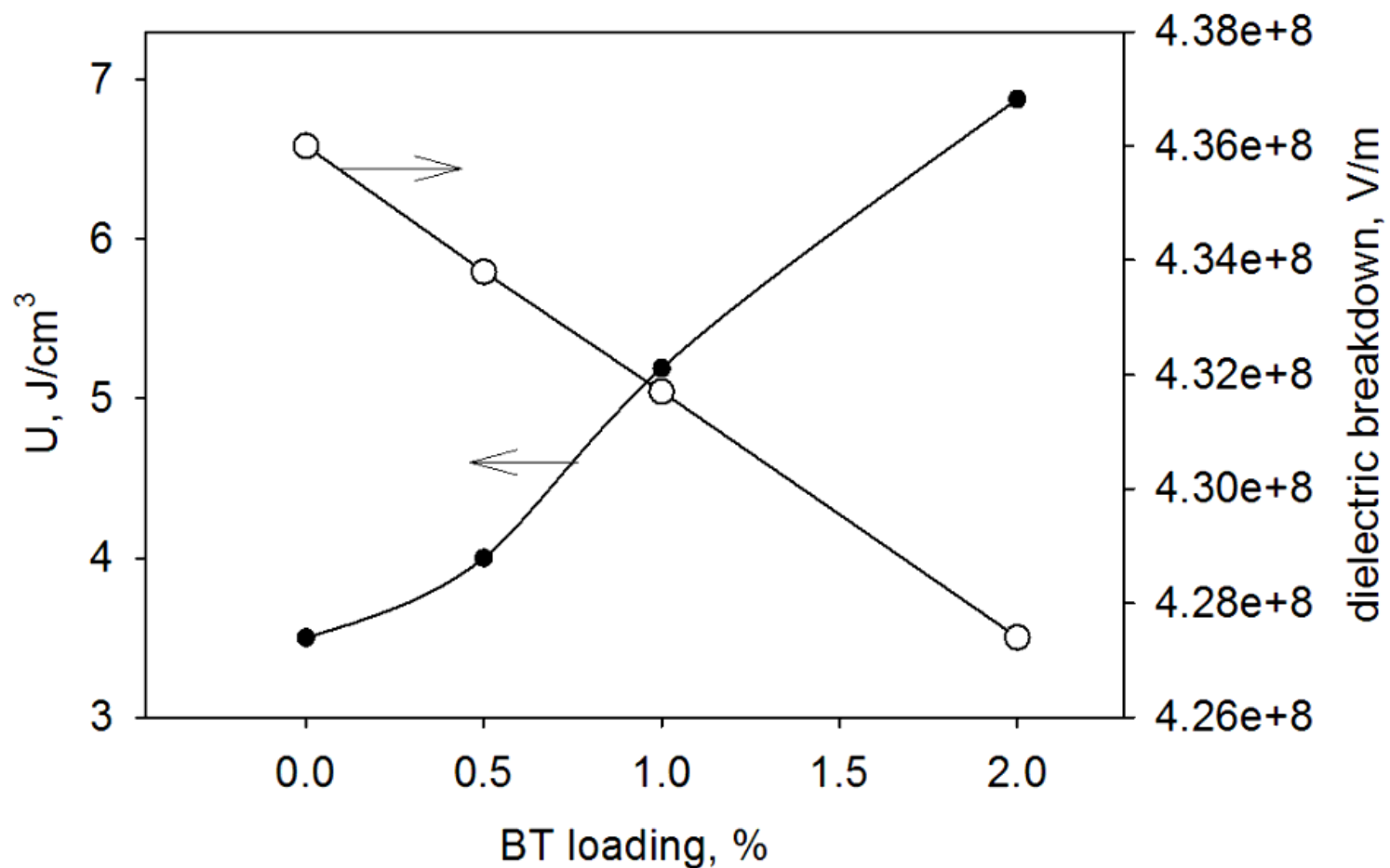


Figure 11

Electric energy density for neat HPC and HPC/BT composites as a function of BT loading